# Shear behaviour of fabric formed T beams reinforced using W-FRP

Yuanzhang YANG[1], John ORR[2*], Tim IBELL[1]

[1] University of Bath, Department of Architectural and Civil Engineering,

BRE Centre for Innovative Construction Materials

Bath, BA2 7AY, UK

[2] University of Cambridge, Department of Engineering,

Cambridge, CB2 1PZ, UK

[*] jjo33@cam.ac.uk

**Abstract**

A combination of flexible moulds as external formwork and bespoke robotically fabricated fibre reinforced polymer cages as tensile reinforcement offers a new opportunity for the manufacture of structural concrete components that have been optimised to minimise material use. This technology could potentially help in our quest to reduce carbon emissions in the construction industry, yet there remain technical issues to overcome if such flexibly formed concrete structures are to become a reality. This paper presents experimental research on fabric-formed T beams reinforced with Wound Fibre-Reinforced Polymer (W-FRP) to quantify the shear contribution of this novel system. It is shown that, depending on the geometry of the beam, carefully chosen flexural and shear reinforcement can resist shear in a predictable manner. Because of geometric variation along the length of the beam, shear resistance is found to move from being provided by both the W-FRP reinforcement and the sloping longitudinal reinforcement to being provided predominantly by the longitudinal FRP reinforcement as the W-FRP gradually ruptures. In turn, this demands higher anchorage capacity of the longitudinal bars than that might have been expected by design codes of practice. By overcoming such issues, this paper shows that savings in concrete of up to 64% can be made in the webs in such structures, compared with conventional T-beams.

**Keyword:** Fabric formwork; Wound FRP; Flexural bar force; Shear resistance.

## 1 Introduction

The UK has recently signed up to the most ambitious carbon-equivalent emissions reductions worldwide, namely to achieve a nearly zero-carbon economy by 2050. Construction needs to play its part in this ambition, more than ever before. The urgency is acute, with a major reduction in carbon emissions and embodied energy being essential (Abergel*, et al.*, 2017, Field, 2014, Orr*, et al.*, 2019). In structural engineering, sustainability of concrete structures has become a more and more important focus as the production of cement contributes to over 5% of annual total carbon emissions around the world due to its large-scale consumption (Boden*, et al.*, 2013).

In conventional reinforced concrete structures, concrete is not fully utilised as the prismatic geometry of concrete components formed by traditional formwork does not match the varying stress resultants caused by the applied loading profile (Orr*, et al.*, 2011, Thirion, 2013). Fabric formwork is a moulding system that uses flexible woven fabrics to support and shape wet concrete (Veenendaal*, et al.*, 2011, West, 2016), by which architecturally interesting and structurally optimised concrete structures can be constructed. Up to 40% concrete savings have been achieved in previous research (Bailiss, 2006, Garbett*, et al.*, 2010), Figure 1.

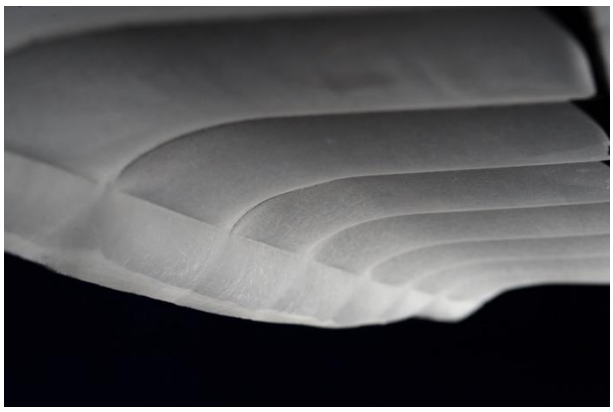

**Figure 1. Fabric formed concrete beam (photo courtesy J Orr)**

However, the non-prismatic geometry of optimised beams can result in complex steel reinforcement cage fabrication. The flexural reinforcement is required to be curved precisely into the design profile and all shear links may have different dimensions (Orr, 2012). By winding flexible fibre filaments coated with resin epoxy around a mandrel, which is itself made of flexible FRP bars, wound fibre-reinforced polymer (W-FRP) shear reinforcement has been developed and applied in concrete beams of either prismatic or non-prismatic geometries, significantly simplifying cage fabrication (Spadea*, et al.*, 2017, Yang*, et al.*, 2018). Although the production of W-FRP could results in much higher carbon emissions than steel (per unit weight), the lightweight of FRP ensures that carbon emission savings can be made (Mara*, et al.*, 2014) by replacing steel reinforcement with FRP.

With flexible formwork and FRP reinforcement, reinforced concrete beams may be formed into complex geometries more conveniently (Kostova, 2016, Veenendaal*, et al.*, 2011, West, 2016). However, such complex geometry and linear-elastic reinforcement could result in different structural behaviour from that of traditional prismatic steel reinforced concrete beams (Hashemian, 2012, Orr, 2012). Due to its variable depth geometry, the inclined flexural reinforcement carries both the flexural tensile force and an additional tensile force created by shear (BSI, 2004, CSA, 2012).

Consequently, the high tensile force in flexural bars at the supports of simply supported non-prismatic beams could potentially result in anchorage failure, limiting the ultimate capacity (Yang, *et al.*, 2018). Therefore, by generating complex geometries, the codified predictions of flexural bar force in the anchorage zones at the ultimate limit state should be examined.

In addition, the positive effect of inclined bars to resist shear is considered in various codes of practice (BSI, 2004, CSA, 2012). This shear contribution relates to the angle of the flexural bars and to the flexural bar force. The codified equations have been extensively validated against prismatic beam tests whilst variations in geometry have not been considered to quantify this positive effect.

This paper presents new experimental research into fabric-formed T beams reinforced with W-FRP reinforcement. Eleven specimens were designed and tested to investigate overall resistance to shear, the enhanced tensile force in the flexural bars and the positive contribution of these bar forces to shear resistance. The contributing factors that determine the flexural bar forces, including choice of W-FRP layout and overall geometric design were considered.

## 2 Methods

The shear capacity, $V_u$, of fabric-formed beams is often calculated using Equation 1, where $V_c$, $V_f$ and $V_t$ are the shear contributions of concrete, shear reinforcement and flexural bars, respectively (Yang, *et al.*, 2018).

$$V_u = V_c + V_f + V_t \quad (1)$$

The positive effect of the inclined flexural reinforcing bars, $V_t$, is the vertical component of the longitudinal reinforcement force at the critical location. This tensile force can be divided into two parts: flexural tensile force and additional tensile force due to shear action. The flexural tensile force can be calculated directly based on simple flexural equilibrium.

The additional tensile force due to shear action can be calculated following Equation 2 and Equation 3 (CSA, 2012). As $V_t$ is related to the flexural bar force, the ultimate shear capacity is calculated iteratively following the method proposed by Yang, *et al.* (2018).

$$T_a = 1.3(V_a - 0.5V_f - V_{tf}) \quad (2)$$

$$V_t = T_a \sin \alpha_t \quad (3)$$

Where, $T_a$ is the additional tensile force; $V_a$ is the applied shear force; $V_{tf}$ is the vertical component of the flexural tensile force and $\alpha_t$ is the angle of the flexural bars to the horizontal axis.

In fabric formed concrete beams, the additional tensile force may be larger than that found in prismatic beams due to the likelihood of a shallower concrete strut angle, coupled with sloping flexural bars. These effects both increase the anchorage forces and could result in premature anchorage failure if not properly accounted for.

In previous research, in which steel bars were used in fabric-formed concrete beams, different types of anchorages were proposed to be welded onto the ends of bars to prevent this potential anchorage failure (Hashemian, 2012, Lee, 2011). But welding is not an option for FRP reinforcement, of course. Instead, a splayed anchorage was adopted to enhance the anchorage strength, as shown

in Figure 2. This system has been shown previously to be highly effective (Darby, *et al.*, 2007, Kostova, *et al.*, 2013, Kostova, 2016).

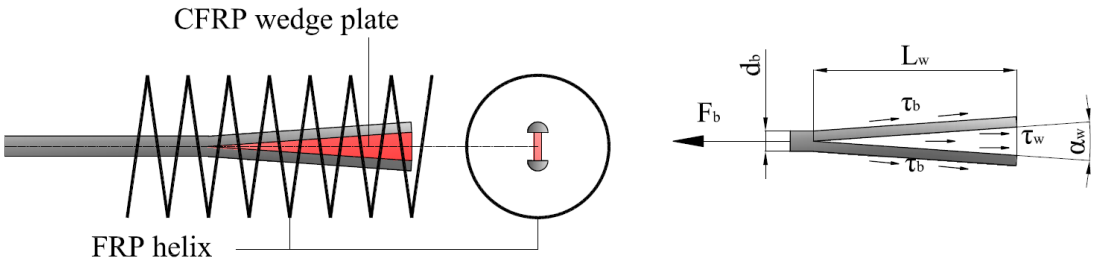


**Figure 2. Splayed anchorage**

The splayed anchorage is formed by making a relatively short longitudinal cut into the FRP bar, splaying its ends, and resining in a carbon wedge plate. An additional FRP helix is used to provide tensile integrity to the surrounding concrete to improve the capacity and ductility of the anchorage. In order to avoid the potential anchorage failure, the design of fabric formed T beams was intended to ensure that the splayed anchorage could provide full anchorage to carry the maximum tensile force in the flexural bars. The strength of the splayed anchorage can be calculated following the work of Kostova (2016), Equation 4.

$$F_b = 1200L_w(\sin\left(\frac{\alpha_w}{2}\right))^2 + 1500mL_w \sin\alpha_w + \tau_w A_w + \tau_b(\pi d_b - 2t_w)L_w \quad (4)$$

where, $F_b$ is the tensile capacity of the splayed anchorage; $L_w$ is the length of splayed anchorage; $\alpha_w$ is the angle of the splay, $m$ is a bond parameter accounting for the nature of the bonding surface; $\tau_w$ is the shear stress on the surface of the carbon wedge; $A_w$ is the two sided area of the carbon wedge; $\tau_b$ is the shear stress on the surface of splayed FRP bar; $d_b$ is the diameter of the splayed bar; $t_w$ is the thickness of the cutting slot (Figure 2).

Following the methods set out here, fabric formed concrete beam specimens reinforced with W-FRP reinforcement were designed to investigate the contributions to shear behaviour resulting from W-FRP shear reinforcement, longitudinal bars and their anchorage arrangements.

## 3 Test program

### 3.1 Specimen design

Eleven simply supported T beam specimens were designed and tested under seven-point bending (Figure 3). This setup was designed to simulate a simply-supported uniformly-loaded precast beam and slab system. The eleven specimens were categorised into six groups (T1 to T6, Table 3) to cover investigations into the effects of overall geometry, W-FRP shear reinforcement and anchorage.

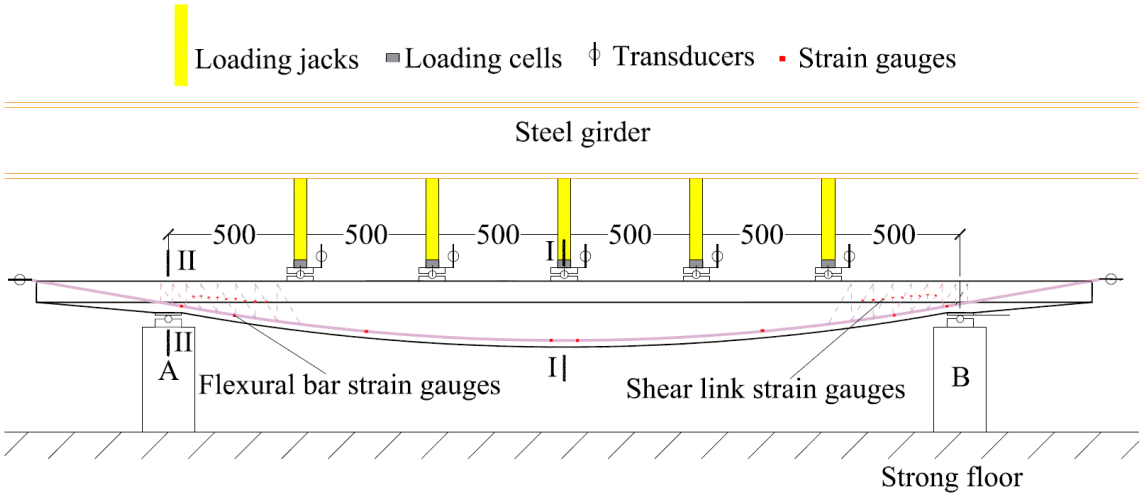


**Figure 3. Test setup and instrumentation**

All the specimens were designed to contain C45/55 concrete, three ø10mm Aslan CFRP flexural bars and W-FRP shear reinforcement. The material properties of flexural and W-FRP shear reinforcement are shown in Table 1, where the W-FRP shear links were wound using multiple layers of 50k SIGRAFIL (SGL Carbon SE, Wiesbaden, Germany) carbon-fibre tow (C T50-4.0/240-E100) with epoxy resin (Fyfe Tyfo S two-component epoxy, San Diego, California).

**Table 1. Material properties of flexural and shear reinforcement (Spadea*, et al.*, 2017)**

| Reinforcement | Cross sectional area $A_f$ (mm2) | Tensile strength $f_{fu}$ (MPa) | Strength at bend corners $f_{fb}$ (MPa) | Tensile strain at corner failure $\varepsilon_{fb}$(%) | Elastic Modulus $E_f$ (GPa) |
|---|---|---|---|---|---|
| W-FRP links | 4.3 | 1537 | 957 | 0.87 | 109 |
| | 8.6 | 1503 | 745 | 0.69 | 108 |
| | 21.4 | 1426 | 654 | 0.62 | 106 |
| ø10 CFRP bar | 71.3 | 2648 | - | - | 143 |

All specimens had the same flange width (800mm), flange depth (80mm) and mid-span cross section I-I (with a depth of 250mm), as shown in Figure 4. As the web width contributes little flexural capacity, the web width was designed to vary from 200mm at the supports to 100mm at mid-span. The web depth along the beam axis was optimised geometrically to cover flexural resistance first, such that every cross section had a flexural resistance higher than, but as close as possible to, the acting bending moment, resulting in a 'bending-moment shape' for a simply supported beam. To cover shear requirements and to investigate these needs in terms of geometry, three different support depths were chosen (varying from 100mm to 180mm) and the resulting geometries were

named as geometry A, B and C. Test groups T1, T2, T2R, T3 and T5 adopted geometry A. Group T4 adopted geometry B and Group T6 adopted geometry C.

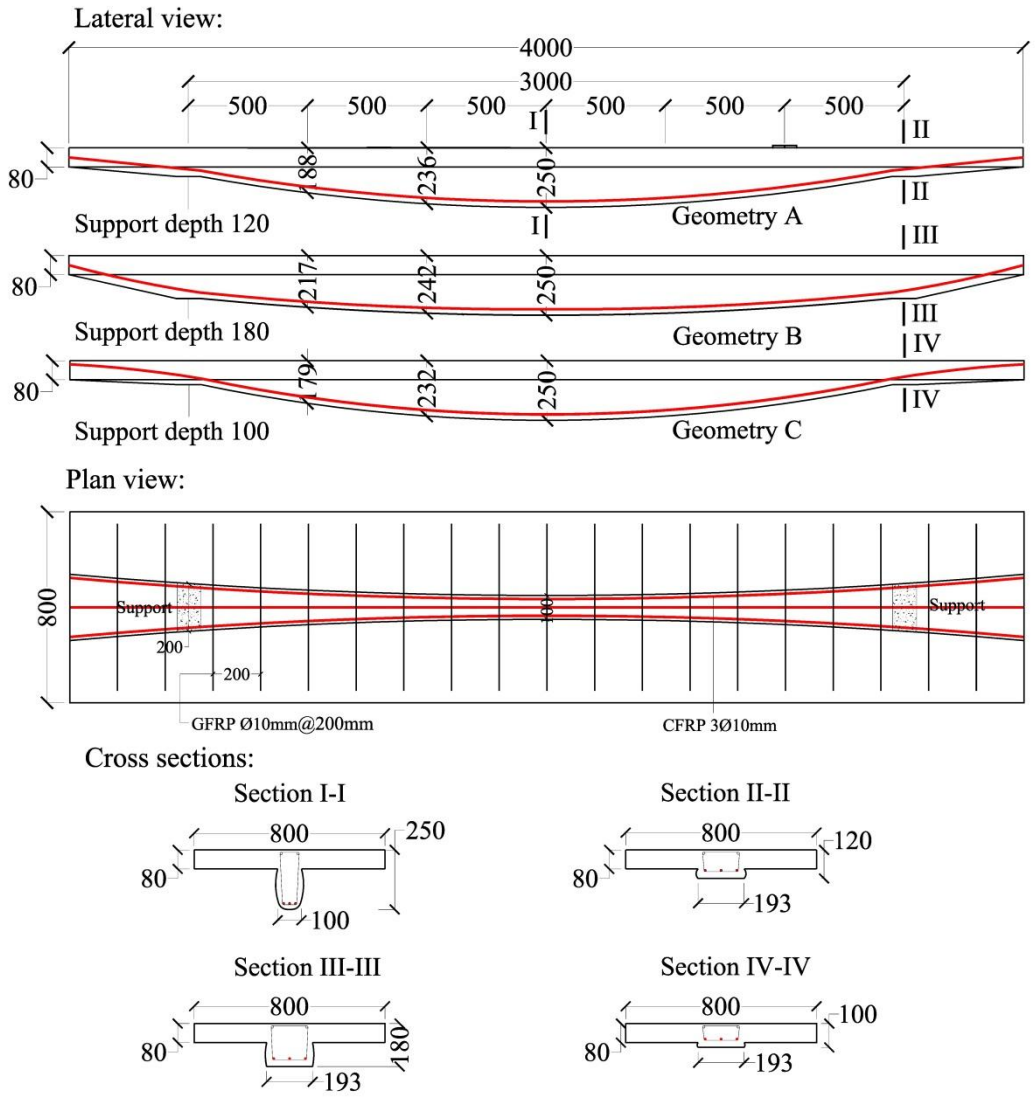


**Figure 4. Geometric design of specimens**

According to previous research (Yang, *et al.*, 2018), the performance of W-FRP in variable depth beams is influenced by both cross-sectional area and patterning of the W-FRP. By varying the arrangement of W-FRP, it is possible to increase shear capacity. To investigate the influence of W-FRP shear reinforcement design, two levels of shear reinforcement ratios and four different W-FRP patterns were designed by varying the cross-sectional area and the inclination of the shear links to the horizontal axis in the shear span, to achieve different shear capacities (Figure 5). By assuming half of the spacing and cross-sectional area, the two specimens in group T2, T2R and T3 had the same shear reinforcement ratio. The coloured W-FRP links of T2-2, T2-2R and T3-2 near the supports (Figure 5) had the same spacing and cross sectional area as the counterparts in T2-1, T2-2R and T3-1, respectively, to allow all aggregates to pass through during casting.

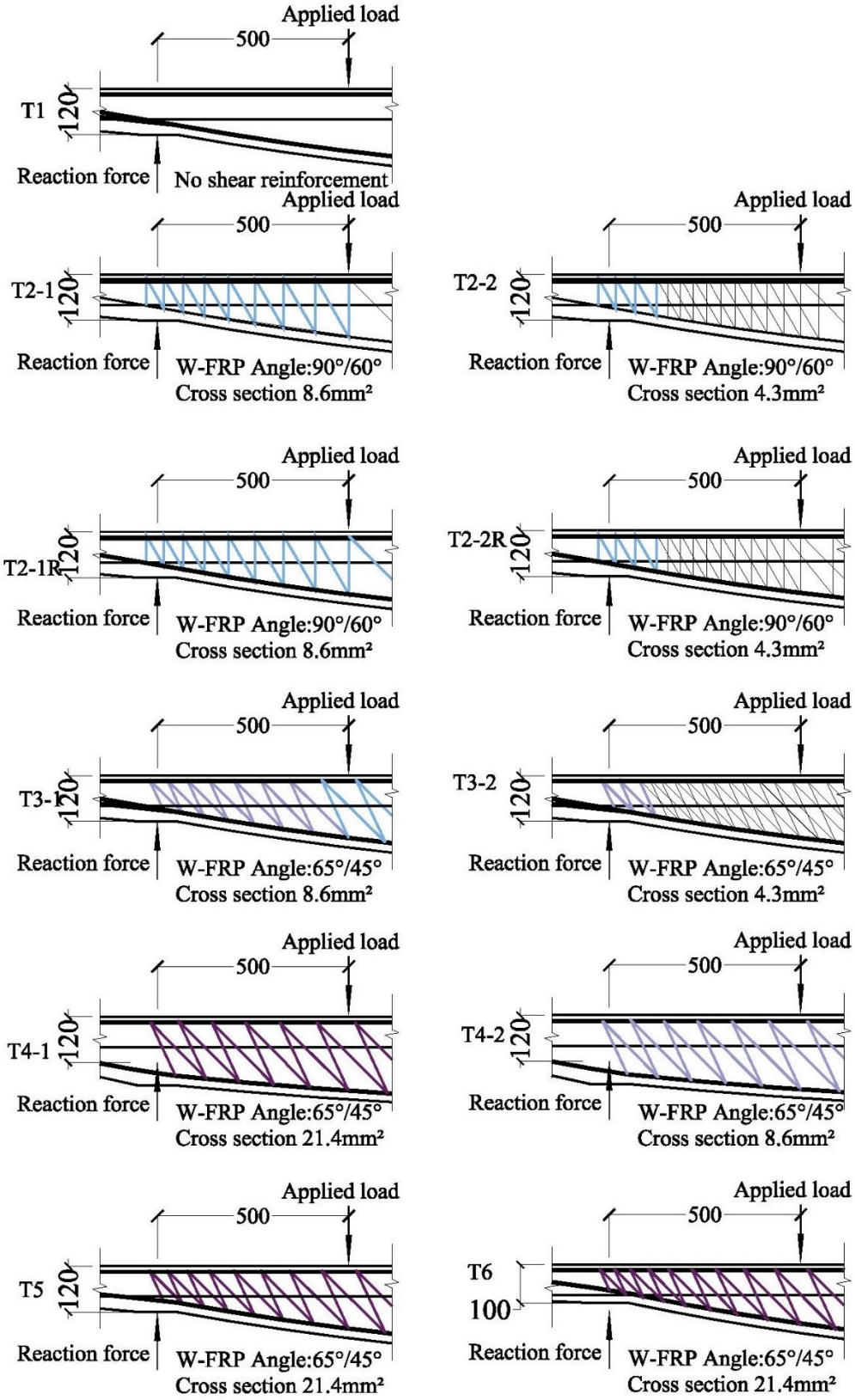


**Figure 5. W-FRP design in the shear span of all specimens**

To simulate the realistic overhangs to support the facade, a 500mm protruding part of the beam slab beyond the support was chosen in all specimens, which also created an anchorage zone to prevent potential end slip failure. Five different anchorage arrangements (Figure 6) were chosen to investigate their effectiveness and influence on the structural behaviour of the specimens. Type I was adopted in specimens T2-1 and T2-2; Type II was adopted in specimens T1, T3-1 and T3-2; Type III was adopted in specimens T2-1R and T2-2R; Type IV was adopted in specimens T4-1 and T5; Type V was adopted in specimens T4-2 and T6. All splayed anchorages had the same 4° splay angle, 100mm splay length and 75mm pitch confining helix. Using Equation 4 (Kostova, 2016), the anchorage strength $R_a$ of each specimen was calculated and compared with the predicted tensile force in the longitudinal bars at the ultimate condition ($T_{ACI}$ and $T_{CSA}$) in Table 2. Based on these calculations, all specimens theoretically had sufficient anchorage strength to prevent anchorage failure.

With this matrix of design assumptions, predictions for all eleven tests in terms of ultimate capacity and failure mode are given in Table 3.

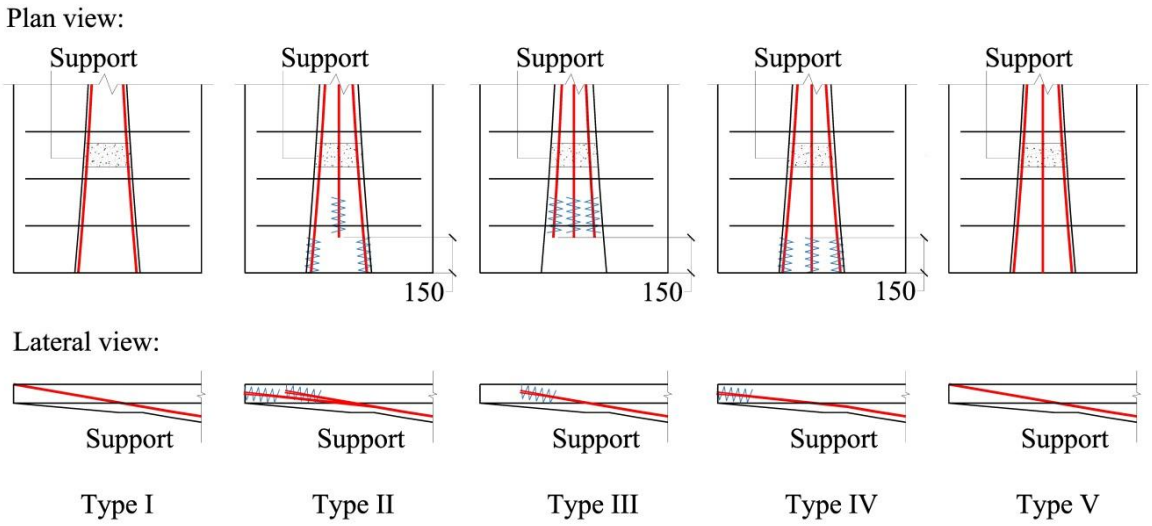


**Figure 6. Anchorage design of specimens**

**Table 2. Predicted anchorage strength and tensile force in flexural bars at ultimate capacity**

| Specimen | $R_a$ (kN) | $T_{ACI}$ (kN) | $T_{CSA}$ (kN) | $R_a/T_{ACI}$ | $R_a/T_{CSA}$ |
|---|---|---|---|---|---|
| T1 | 525 | 171 | 168 | 3.1 | 3.2 |
| T2 | 206 | 152 | 138 | 1.4 | 1.5 |
| T2R | 464 | 152 | 138 | 3.1 | 3.4 |
| T3 | 525 | 152 | 138 | 3.5 | 3.8 |
| T4-1 | 556 | 116 | 103 | 4.8 | 5.5 |
| T4-2 | 309 | 149 | 133 | 2.1 | 2.3 |

| | | | | | |
|---|---|---|---|---|---|
| T5 | 556 | 124 | 100 | 4.5 | 5.5 |
| T6 | 309 | 131 | 117 | 2.4 | 2.6 |

**Table 3. Design summary of all specimens**

| Specimen | Geometry Type | Shear design | | | Anchorage type | Predicted failure load (and mode) | |
|---|---|---|---|---|---|---|---|
| | | Shear reinforcement ratio $\rho_{fv}$ (%) | Angles of shear links $\alpha_1/\alpha_2$ (°) | Cross section area $A_{fv}$ (mm$^2$) | | ACI 440.1 (kN) | CSA S806 (kN) |
| T1 | A | - | - | - | II | 33 (S) | 47 (S) |
| T2-1 | A | 0.34 | 60/90 | 8.6 | I | 105 (S) | 200 (S) |
| T2-2 | A | 0.34 | 60/90 | 4.3 | I | 105 (S) | 200 (S) |
| T2-1R | A | 0.34 | 60/90 | 8.6 | III | 105 (S) | 200 (S) |
| T2-2R | A | 0.34 | 60/90 | 4.3 | III | 105 (S) | 200 (S) |
| T3-1 | A | 0.34 | 45/65 | 5.6 | II | 105 (S) | 200 (S) |
| T3-2 | A | 0.34 | 45/65 | 4.3 | II | 105 (S) | 200 (S) |
| T4-1 | B | 0.64 | 45/65 | 21.4 | IV | 221 (S) | 258 (F) |
| T4-2 | B | 0.26 | 45/65 | 8.6 | V | 111 (S) | 199 (S) |
| T5 | A | 0.85 | 45/65 | 21.4 | IV | 213 (S) | 258 (F) |
| T6 | C | 0.87 | 45/65 | 21.4 | V | 193 (S) | 258 (F) |

Note: 1. S denotes shear failure and F denotes flexural failure.

2. The flexural capacity prediction following ACI 440.1 (2015) is 263kN.

### 3.2 Specimen fabrication

Instead of using a hand-winding method adopted in previous research (Spadea*, et al.*, 2017, Yang*, et al.*, 2018), the W-FRP cage for each specimen was fabricated using an automated semi-robotic winding machine. After curing of the FRP cages, all specimens were cast in fabric formwork.

During testing, it was found that specimen T3-1 had failed due to end slip of the flexural bars beyond the support. To avoid the same failure mode in the testing of specimen T3-2, additional mechanical anchorages (Figure 7) were installed on the protruding splayed bars to further enhance the anchorage strength.

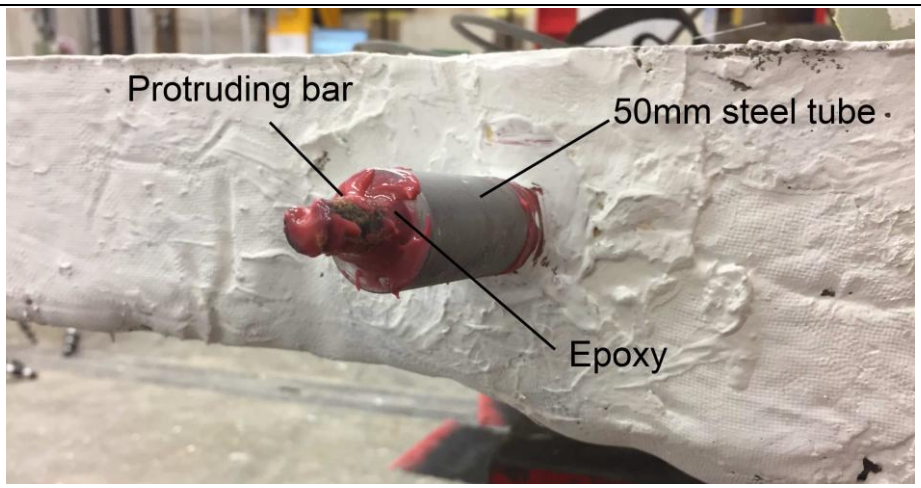


**Figure 7. Mechanical anchorage installed on specimen T3-2**

### 3.3 Instrumentation

To understand how the tensile force in the longitudinal bars develops at the supports, strain gauges were installed on the flexural reinforcement and shear reinforcement in the shear span. Transducers were placed at the loading jacks and at the ends of protruding flexural bars to record displacements. All instrumentation is shown in Figure 3.

### 3.4 Concrete strength

The concrete strength was determined on the day of testing. Five cubes and three cylinders were cast and tested to determine the concrete strength for each specimen following BS EN 12390-1(BSI, 2012) and BS EN 12390-3 (BSI, 2009), respectively. Group T2 was cast using ready-mix concrete (C45/C55) and tested at 28 days. Due to the unexpectedly low concrete strength (Table 4), all other specimens were cast using laboratory-mixed concrete with a target mean strength of 58MPa at 10 days (Teychenné, *et al.*, 1975), due to the laboratory schedule. The resulting concrete cylinder strengths $f_c$ and cube strengths $f_{cu}$ are shown in Table 4.

**Table 4. Concrete strength of each specimen**

| specimen | T1 | T2-1 | T2-2 | T2-1R | T2-2R | T3-1 | T3-2 | T4-1 | T4-2 | T5 | T6 |
|---|---|---|---|---|---|---|---|---|---|---|---|
| $f_c$ (MPa) | 40.6 | 28.4 | 28.4 | 37.6 | 42.0 | 44.0 | 47.1 | 44.0 | 47.5 | 49.2 | 51.8 |
| $f_{cu}$ (MPa) | 50.0 | 31.6 | 31.6 | 41.3 | 47.9 | 44.2 | 49.1 | 48.3 | 55.1 | 53.7 | 52.7 |

### 3.5 Results

#### 3.5.1 Summary

All specimens were tested until failure in loading increments of 10kN (2kN per jack). The test setup is shown in Figure 3. Three types of failure modes were observed from the tests: i) flexural failure, ii) shear failure and iii) end-slip failure of the longitudinal bars. A summary of the test results is shown in Table 5. Load-deflection curves of the specimens are shown in Figure 8. The specimens were designed in line with empirical equations from ACI 440.1 (2015) and CSA S806 (2012). These empirical equations from the codes of practice were formulated based on experimental research on

prismatic concrete elements. This raises important and interesting issues associated with inherent presumptions made in the formulation of codified rules, but this is beyond the scope of this paper. To help, however, the paper includes expected failure modes in order to assist with comparisons.

**Table 5. Test results summary**

| Specimen | Total applied load at failure $P_{u,exp}$ (kN) | Mid-span deflection (mm) | Expected failure mode (ACI 440.1) | Expected failure mode (CSA S806) | Experimental failure mode |
|---|---|---|---|---|---|
| T1 | 101 | 45 | Shear | Shear | Shear |
| T2-1 | 153 | 100 | Shear | Shear | End slip |
| T2-2 | 160 | 109 | Shear | Shear | End slip |
| T2-1R | 188 | 80 | Shear | Shear | Shear |
| T2-2R | 222 | 100 | Shear | Shear | End slip |
| T3-1 | 226 | 95 | Shear | Shear | End slip |
| T3-2 | 253 | 120 | Shear | Shear | Flexure |
| T4-1 | 279 | 107 | Shear | Flexure | Flexure |
| T4-2 | 217 | 90 | Shear | Shear | End slip |
| T5 | 261 | 117 | Shear | Flexure | Flexure |
| T6 | 233 | 110 | Shear | Flexure | Flexure |

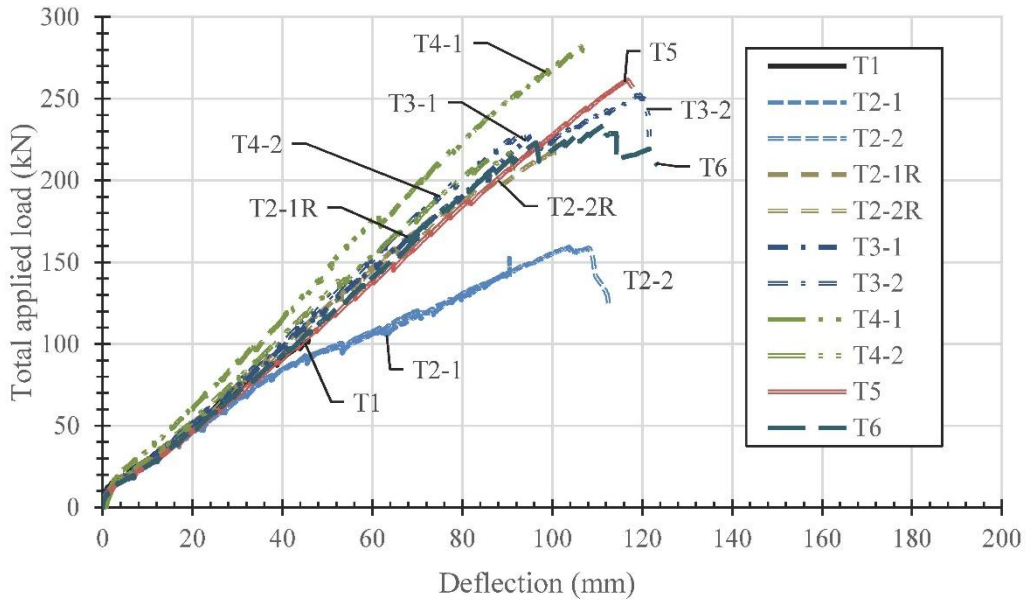


**Figure 8. Load-deflection curves of all specimens**

### 3.5.1 Failure mode

Specimens T1 and T2-1R failed in shear (Figure 9), as expected. Flexural failure was observed in specimens T3-2, T4-1, T5 and T6, as shown in Figure 10. Although W-FRP shear link rupturing and flexural bar end slip were observed in specimen T3-2, it finally failed by flexural bar rupturing at mid-span, which was also observed in T4-1 and T5. T6 failed by concrete crushing beneath the loading jack next to support B (Figure 3).

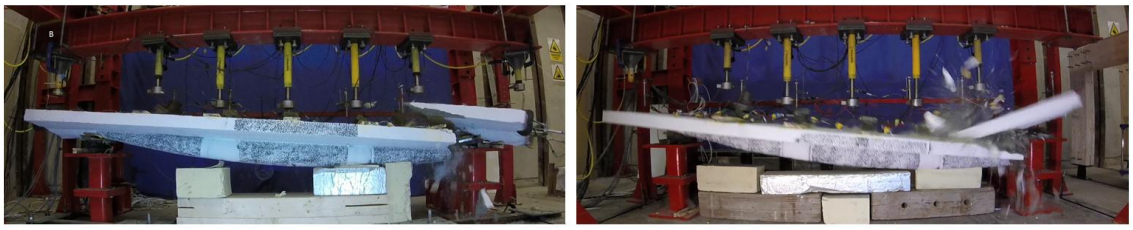


**Figure 9. Shear failure of specimens T1 and T2-1R**

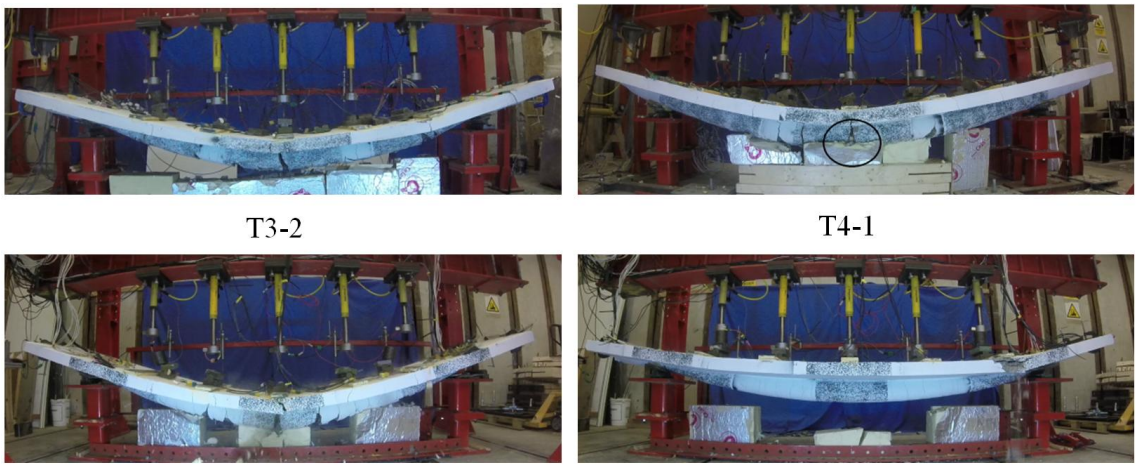


**Figure 10. Flexural failure of specimens T3-2, T4-1, T5 and T6**

Although specimens T2-1, T2-2, T2-2R, T3-1 and T4-2 were predicted to fail in shear (Table 3) and were designed to have sufficient anchorage strength (Table 2), end slip failure occurred (Figure 11) as the protruding flexural bars were pulled into the flange. The end slip of flexural bars in most of these specimens was only observed after a progression of shear link ruptures.

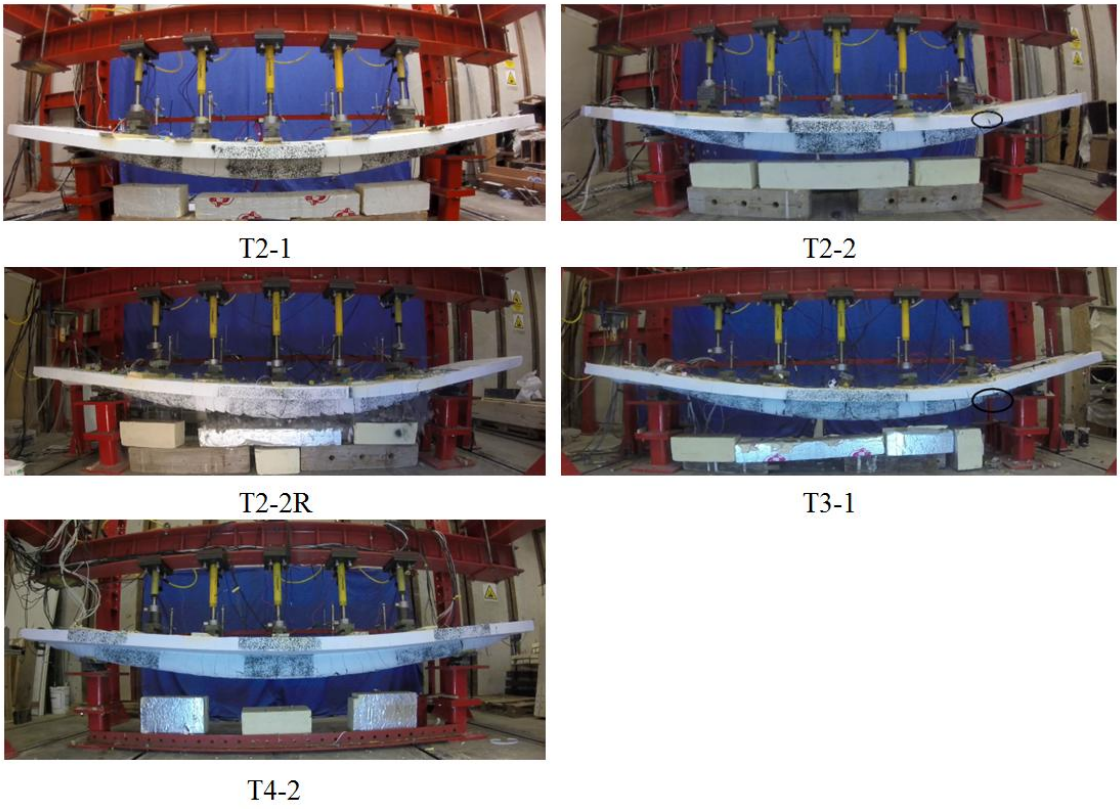


**Figure 11. End slip failure of specimens T2-1, T2-2, T2-2R, T3-1 and T4-2**

Although there was no repetition of each specimen in this research, the end-slip failure mode was seen consistently across many specimens. The load-deflection curves (Figure 8) and the strain development in flexural bars at the support area (see section 3.5.2) show good consistency, adding confidence to the reliability of the test results.

Under increasing load, large displacement of the specimens resulted in significant rotations at the supports (Figure 12). Rotation at the support created large slopes of the flexural bars (Figure 4) and changed the angles of W-FRP links to the horizontal axis (Figure 5) compared with the initial design. Support rotation varied from 5° to 9° across specimens at ultimate capacity.

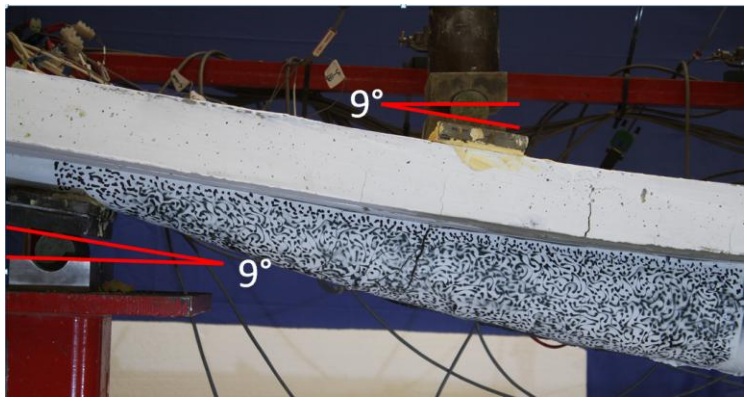


**Figure 12. Rotation of a support of specimen T3-2**

### 3.5.2 Strain in flexural bars

The load-strain curves for the longitudinal bars close to a support are shown in Figure 13, where με stands for micro-strain. For specimens which encountered end slip of flexural bars, the strain in the flexural bars exceeded the gauge range limit and, therefore, no reading was recorded at final failure of the specimens. As each flexural bar was gauged, the strain in Figure 13 is taken as the average value across three readings in each case.

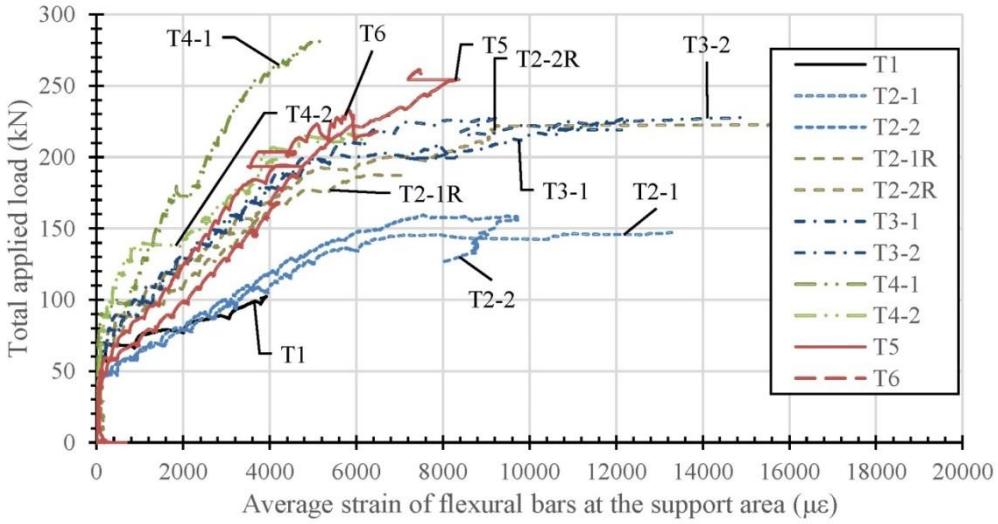


**Figure 13. Average strains of flexural reinforcement at supports**

## 4 Analysis

### 4.1 Shear contribution of flexural and shear reinforcement

The shear contribution of both flexural and shear reinforcement in the shear span is assessed by calculating the vertical component of the tensile force in the shear links and flexural reinforcement crossing the primary shear crack. Using the flexural and shear reinforcement strain and their actual angles to the horizontal axis, the shear contributions of the flexural and shear reinforcement prior to shear link rupture are presented in Table 6.

**Table 6. Shear contributions of flexural and shear reinforcement before shear link rupture**

| Specimen | T1 | T2-1 | T2-2 | T2-1R | T2-2R | T3-1 | T3-2 | T4-1 | T4-2 | T5 | T6 |
|---|---|---|---|---|---|---|---|---|---|---|---|
| $V_a$ (kN) | 51.0 | 73.0 | 73.0 | 94.0 | 94.0 | 94.0 | 94.0 | 140.0 | 94.0 | 129.0 | 107.0 |
| $V_f$ (kN) | - | 27.4 | 37.4 | 37.5 | 44.3 | 38.5 | 32.1 | 103.0 | 49.7 | 55.1 | 39.0 |
| $V_f/V_a$ | - | 0.38 | 0.51 | 0.40 | 0.47 | 0.41 | 0.34 | 0.74 | 0.51 | 0.42 | 0.37 |
| $V_t$ (kN) | 22.6 | 40.3 | 34.9 | 42.5 | 35.7 | 35.7 | 38.3 | 35.2 | 27.7 | 71.0 | 60.2 |
| $V_t/V_a$ | 0.44 | 0.55 | 0.48 | 0.45 | 0.38 | 0.38 | 0.41 | 0.25 | 0.29 | 0.55 | 0.57 |

| | | | | | | | | | | | |
|---|---|---|---|---|---|---|---|---|---|---|---|
| $V_f/V_t$ | - | 0.68 | 1.07 | 0.88 | 1.24 | 1.08 | 0.84 | 2.92 | 1.80 | 0.77 | 0.65 |
| $V_r/V_a$ | 0.44 | 0.93 | 0.99 | 0.85 | 0.86 | 0.79 | 0.75 | 0.99 | 0.82 | 0.98 | 0.94 |

where, $V_a$ is the applied shear force near a support, taken as half of the applied load; $V_f$ is the shear contribution of W-FRP shear links; $V_t$ is the shear contribution of flexural bars; $V_r$ is the sum of $V_f$ and $V_t$.

It is found that the shear reinforcement and flexural reinforcement provided most of the total shear resistance (Table 6). Before shear link rupture, the flexural reinforcement provided a similar, or higher, shear contribution compared with the W-FRP shear links in the specimens with geometry A (all specimens excluding T4 and T6), shown by the ratio of shear contribution of shear reinforcement to flexural reinforcement $V_f/V_t$ varying from 0.68 (T2-1) to 1.24 (T2-2R) with an average value of 0.90 and a standard deviation of 0.19. For specimens T4-1 and T4-2 of geometry B, the shear reinforcement provided a larger shear contribution than the flexural bars. Yet the shear contribution of shear reinforcement still reaches over 25% of the total applied shear force, Table 6. In specimen T6 of geometry C, $V_t/V_a$ reaches 0.57, demonstrating that in this situation the flexural reinforcement provided the majority of resistance to shear. This indicates that unlike in prismatic beams, the flexural reinforcement of the specimens can be effectively utilised to carry the applied shear force.

After rupture of W-FRP shear links, load redistribution from W-FRP to longitudinal reinforcement occurred. As shown in Figure 14, at the point of shear link rupture, an abrupt decrease in contribution from shear reinforcement and a simultaneous increase in contribution from flexural bars to shear were recorded. Rupturing of a section of shear links did not result immediately in shear failure of the specimens as the force in the inclined bars increased to carry the majority of the shear force. The increased tensile force in the flexural bars as a result of this led to end slip failure of these bars. The final failure load and mode are governed by the anchorage design, highlighted by the comparison between specimen T3-2, in which an additional mechanical anchorage was installed on each of the protruding flexural bars, and the remaining end-slip failure specimens.

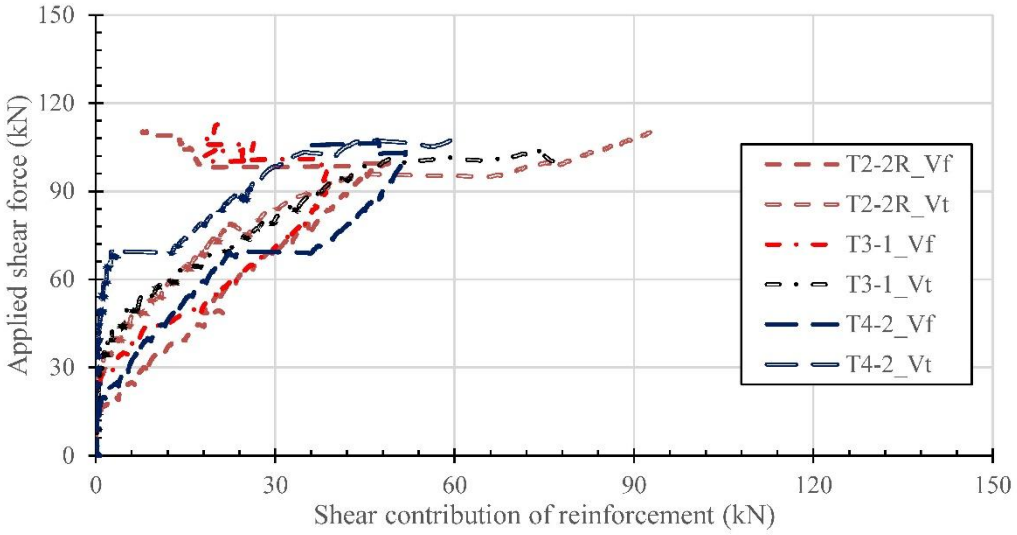


**Figure 14. Shear contribution of flexural and shear reinforcement in T2-2R, T3-1 and T4-2**

Although specimens T2-1 and T2-2 show lower stiffness and failure load, similar load redistributions can be observed between the flexural bars and shear links, Figure 15. There were only two flexural bars anchored beyond the support (Figure 6) to carry both the flexural and addition tensile forces, which resulted in lower stiffness (Figure 8) hence larger support rotations and hence larger tensile strains in flexural bars (Figure 13). The resulting shear contribution of flexural bars in specimens T2-1 and T2-2 is similar to the other specimens with geometry A. Due to the lower anchorage strength and higher tensile force in flexural bars, T2-1 and T2-2 failed at a much lower total applied load compared with the other specimens.

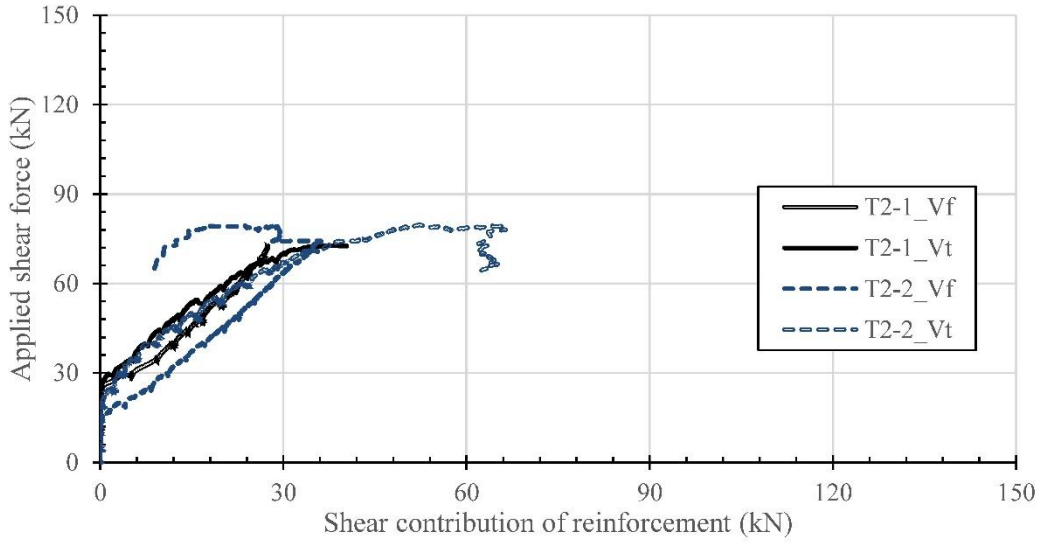


**Figure 15. Shear contribution of flexural and shear reinforcement in T2-1 and T2-2**

## 4.2 Geometry

Specimen geometry was found to influence the flexural bar force in relation to the angle between concrete and flexural reinforcement. All beams had a smaller support depth compared with that of the prismatic beams, which results in shallower concrete strut angle and larger angle of flexural bars, as shown in Figure 16. The smaller support depth also reduces the stiffness of the specimens and creates larger support rotations, hence leading to still smaller concrete strut angles and larger angles of flexural bars. Consequently, the additional tensile force and its vertical component created by shear increases according to Equations 2 and 3, as shown in Table 6.

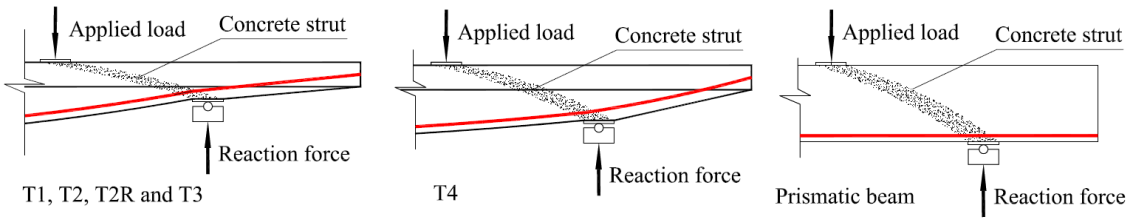


**Figure 16. Concrete strut angle of specimens with different geometries**

In prismatic beams, the shear link rupture directly causes shear failure, whilst for most of the specimens designed for shear failure, the non-prismatic geometries creates the preliminary

condition for load redistribution. That is the sloping flexural bars are able to provide sufficient shear contribution to make up for the loss of W-FRP links. Due to this load redistribution, the expected brittle shear failure was transformed into a non-brittle end-slip failure where the specimens exhibited apparent non-linear load-deflection behaviour between initial shear link rupture and final end-slip failure (Figure 8). This higher deformability is desirable in FRP-reinforced concrete structural design.

The use of a tapered beam may allow more efficient use of concrete. Comparisons between the test specimens and a reference prismatic T beam with an equivalent flexural capacity, exhibiting mid-span depth of 250mm, 800mm flange width, 80mm flange depth and 200mm web width, are shown in Table 7. The ratio of $Q_{c,web}$ varies from 0.36 to 0.59, indicating concrete savings in the web ranging from 41% to 64% through the use of a non-prismatic geometry. The total concrete saving varies from 15% to 23%, as much of the concrete is in the flange. The top flange of the specimens was designed to simulate the slab in a normal concrete building and there is a potential to further increase concrete savings by optimizing the flange design (Hawkins*, et al.*, 2017).

**Table 7. Concrete use comparison**

| Geometry | $Q_{c,web}$ (m3) | $Q_{c,flange}$(m3) | $Q_c$ (m3) | Ratio of $Q_{c,web}$ | Ratio of $Q_{c,flange}$ | Ratio of $Q_c$ |
|---|---|---|---|---|---|---|
| A | 0.056 | 0.256 | 0.312 | 0.42 | 1.00 | 0.80 |
| B | 0.080 | 0.256 | 0.336 | 0.59 | 1.00 | 0.85 |
| C | 0.048 | 0.256 | 0.305 | 0.36 | 1.00 | 0.77 |
| Reference | 0.136 | 0.256 | 0.391 | 1.00 | 1.00 | 1.00 |

where, $Q_{c,web}$is the concrete of volume in the specimen web, $Q_{c,flange}$ is the volume of concrete in the specimen flange and $Q_c$ is the total volume of concrete used in each specimen.

### 4.3 W-FRP shear reinforcement

The test results demonstrate that both optimising the W-FRP pattern and increasing the shear reinforcement ratio can enhance the load at which shear link rupture occurs. A higher shear reinforcement ratio enhances the shear contribution of the W-FRP shear links and hence the shear contribution of flexural bars, shown by the comparisons amongst specimens T1, T3-1 and T5 (Table 6).

The W-FRP pattern of T3-2 has been shown to be the optimal pattern among all the specimens that encountered shear link rupture, achieving the highest applied load at link rupture of 220kN. By reducing the cross-sectional area and spacing, the W-FRP links in T3-2 had a smaller radius at the corner and equivalent diameter than those in T3-1, contributing to higher corner strength, Table 1. Compared with specimens T2-1, T2-1R and T3-1, the higher strength of shear reinforcement could be the critical reason for the highest link rupturing load occurring in T3-2.

Unlike steel stirrups that can all yield prior to shear failure, FRP is a linear-elastic material and the tensile strain in each link will not necessarily reach the same value prior to rupture. Differences in

strain between adjacent links are related to their angle of inclination. For example, specimen T3-2 had a smaller angle difference between adjacent links compared with specimen T2-2R (Figure 5), and thus there was a higher probability of adjacent links reaching similar strains at failure. This may help to avoid particular shear links rupturing while their neighbouring links still have low strains, and thus the W-FRP can be more effectively utilised.

FRP is a unidirectional material with high axial tensile strength and low transverse shear strength. When diagonal shear cracks open, any links not perpendicular to the shear cracks will carry some local shear force. The W-FRP links with larger inclinations in specimen T3-2 were more likely to be perpendicular to the shear cracks and hence could reduce the influence of local shear force on the links during the opening of shear cracks.

When the shear links are arranged in the optimal pattern at 45°and 65°angles to the horizontal axis and a cross-sectional area of 4.3mm$^2$ is used, it is feasible to construct non-prismatic beams according to minimum shear reinforcement with full shear capacity being ensured.

### 4.4 Prediction examination

#### 4.4.1 Ultimate capacity

Comparisons between predictions made using design codes and the test results are shown in Table 8. ACI 440.1 (2015) gives conservative predictions in all cases, with an average $P_{u,exp}/P_{u,ACI}$ ratio of 1.83 and a standard deviation of 0.58. This conservatism is unlikely to assist the designer in minimising concrete material use. CSA S806 (2012) provides more accurate predictions ($P_{u,exp}/P_{u,CSA} = 1.11$) with a smaller standard deviation of 0.37.

**Table 8. Predictions comparisons**

| Specimen | $P_{u,exp}$ (kN) | $P_{u,ACI}$ (kN) | $P_{u,CSA}$ (kN) | $P_{u,exp}/P_{u,ACI}$ | $P_{u,exp}/P_{u,CSA}$ |
|---|---|---|---|---|---|
| T1 | 101 | 33 | 47 | 3.06 | 2.14 |
| T2-1 | 153 | 105 | 200 | 1.45 | 0.77 |
| T2-2 | 160 | 105 | 200 | 1.52 | 0.80 |
| T2-1R | 188 | 105 | 200 | 1.79 | 0.94 |
| T2-2R | 222 | 105 | 200 | 2.11 | 1.11 |
| T3-1 | 226 | 105 | 200 | 2.15 | 1.13 |
| T3-2 | 253 | 105 | 200 | 2.41 | 1.26 |
| T4-1 | 279 | 221 | 258 | 1.26 | 1.08 |
| T4-2 | 217 | 111 | 199 | 1.95 | 1.09 |
| T5 | 261 | 213 | 258 | 1.22 | 1.01 |
| T6 | 233 | 193 | 258 | 1.20 | 0.90 |

| | | |
|---|---|---|
| Average | 1.83 | 1.11 |
| SD | 0.58 | 0.37 |

where, $P_{u,exp}$ is the total applied load at ultimate failure, $P_{u,ACI}$ is the total load prediction using ACI440.1 (2015) at ultimate failure and $P_{u,CSA}$ is the total load prediction using CSA S806 (2012) at ultimate failure.

### 4.4.2 W-FRP

The shear contribution predictions of W-FRP ($V_f$) can only be examined for the specimens which encountered link rupture. Therefore the predictions of $V_f$ in specimens T2, T3 and T4-2 are compared with test results in Table 9. CSA S806 (2012) gives relatively accurate but unconservative predictions, whilst ACI 440.1 (2015) underestimates the W-FRP shear contribution by over 30%.

The different ratios of $V_f/V_{f,ACI}$ and $V_f/V_{f,CSA}$ are mainly governed by two criteria: the concrete strut angle $\theta$ and the design strength of shear links. CSA adopts a variable angle truss model, where $\theta$ for all specimens is smaller than 45° whilst ACI adopts a constant concrete strut angle of 45°. This results in larger values of cot(θ) calculated following CSA S806 (2012). In addition, the design strength of W-FRP of the CSA predictions is governed by the 0.5% ultimate strain, which is higher than the 0.4% ultimate strain of ACI (2015) predictions. Due to the larger concrete strut angle and smaller design strength of W-FRP links, ACI predictions are more conservative than the CSA predictions.

**Table 9. Comparison of W-FRP shear contribution**

| Specimen | $V_f$(kN) | $V_{f,ACI}$ (kN) | $V_{f,CSA}$ (kN) | $V_f/V_{f,ACI}$ | $V_f/V_{f,CSA}$ |
|---|---|---|---|---|---|
| T2-R | 37.5 | 29.1 | 41.8 | 1.29 | 0.90 |
| T2-2R | 44.3 | 29.1 | 41.8 | 1.52 | 1.06 |
| T3-1 | 38.5 | 29.1 | 41.8 | 1.32 | 0.92 |
| T3-2 | 32.1 | 29.1 | 41.8 | 1.10 | 0.77 |
| T4-2 | 49.7 | 34.3 | 49.7 | 1.45 | 1.01 |
| Average | | | | 1.34 | 0.93 |
| SD | | | | 0.16 | 0.11 |

where, $V_{f,ACI}$ and $V_{f,CSA}$ are predictions of the W-FRP shear contribution according to ACI 440.1 (2015) and CSA S806 (2012), respectively.

### 4.4.3 Flexural bars

The predictions for the ratio of the shear contribution of flexural bars to shear capacity are compared with the test results (before shear link rupture) in Table 10. Both ACI440.1 (2015) and CSA

S806 (2012) underestimate the shear contribution of flexural bars, highlighted by the experimentally determined ratio of $V_t/V_a$ being approximately twice that of the predictions.

**Table 10. Comparison of flexural reinforcement shear contribution**

| Specimen | $V_t/V_a$ | $V_{t,ACI}/V_{u,ACI}$ | $V_{t,CSA}/V_{u,CSA}$. |
|---|---|---|---|
| T1 | 0.44 | 0.28 | 0.28 |
| T2, T2R, T3 | 0.44 | 0.22 | 0.24 |
| T4 | 0.27 | 0.10 | 0.12 |
| T5 | 0.55 | 0.21 | 0.23 |
| T6 | 0.57 | 0.25 | 0.29 |

where, $V_{t,ACI}$ and $V_{u,ACI}$ are predictions of flexural reinforcement shear contribution and shear capacity according to ACI 440.1 (2015), respectively and $V_{t,CSA}$ and $V_{u,CSA}$ are predictions of flexural reinforcement shear contribution and shear capacity according to CSA S806 (2012), respectively.

The underestimation of flexural bar force and shear contribution could be attributed to a codified design approach which is itself based implicitly on test data involving prismatic structures, in the main. For FRP-reinforced concrete beams, CSA specifies $\cot\theta$ in Equation 2 as a constant value of 1.3, indicating that the concrete strut angle $\theta$ is assumed to be 52°. However, the angle of the concrete strut of the test specimens was found to be much lower. Assuming that the load is transferred from the loading point to the support through a straight concrete strut (Figure 16), the concrete strut angle in specimens with geometry A reaching as low as 13°. The shallower support depth could increase the value of $\cot\theta$ and hence the additional tensile force according to Equation 2.

CSA does allow inclined flexural bars to contribute to shear. However, the influence of support rotation on this shear contribution is not stipulated. For prismatic beams, this may not be an issue, but for the tapered geometries tested here, rotation of the supports can result in a 5-9° angle change. The angles of the concrete strut and flexural bars to the horizontal axis will change accordingly, which can significantly increase the flexural bar force and its vertical component.

CSA does not consider the load redistribution from shear links to flexural bars for FRP-reinforced beams. However, redistribution is indeed seen in the specimens designed for shear failure. The high tensile strains in the flexural bars (over 1.4%) as shown in Figure 13 as the result of this lead to the underestimation of flexural bar force after link rupture.

Such underestimation in tensile force in the flexural bars following Equation 2 could potentially result in an unsafe design of the anchorage, shown by the pull-out of splayed anchorages in the specimens designed for shear failure. When the anchorage is properly designed, the underestimation of flexural bar force could also results in an underestimation of ultimate capacity, highlighted by the highly conservative predictions for T1 (Table 8), which in turn is not helpful to minimise material use. This indicates that further revisions to the existing design method are

required to formulate a design process for non-prismatic beams, which can model flexural bar force development as part of the full loading process to accurately predict the correct failure mode and ultimate capacity.

## 5 Conclusions

This paper investigated the shear behaviour of W-FRP reinforced non-prismatic simply supported T-beams through the testing and subsequent analysis of eleven test specimens. The research supports the following conclusions:

1. Fabric formed T beams with W-FRP reinforcement are susceptible to end-slip failure of the flexural bars, initiated by extremely high tensile forces caused by gradual rupturing of shear links. Such rupturing does not necessarily cause direct shear failure but load redistribution from shear links to flexural bars.
2. Sloping flexural reinforcement carries anything up to half of the applied shear force, particularly after shear link rupture when redistribution occurs.
3. Geometric design of fabric formed beams is the major factor that influences overall structural behaviour. By reducing the depth at the support area, fabric formed beams will have lower stiffness, shallower concrete strut angle and a larger slope in their flexural bars, all of which enhance the flexural bar force and the corresponding shear contribution.
4. The CSA S806 (2012) equation to calculate the flexural bar force cannot accurately predict the bar force in beams with variable-depth geometries due to overestimation of the concrete strut angle and omission of the support rotation. Unexpected load redistribution makes the prediction even less accurate. This research has shown, for the first time, that deficiencies exist in codified approaches when dealing with tapered structures, possibly because the approaches are themselves not based on relevant experimental evidence.
5. Compared with an equivalent T beam, fabric formed T beams could save up to 64% concrete in the web, and up to 23% concrete overall. More potential material savings could be made by optimising the flange geometry.

**Acknowledgement**

The authors acknowledge and are grateful for the support of the BRE CICM (www.bath.ac.uk/bre), the University of Bath, EPSRC and China Scholarship Council who collectively funded the PhD position that has resulted in this work. Funding for experimental work from EPSRC grant EP/M020908/1 is acknowledged.

**References**

Abergel, T., Dean, B., and Dulac, J. (2017). "Towards a zero-emission, efficient, and resilient buildings and construction sector: Global Status Report 2017." UN Environment: International Energy Agency, Paris, France.

ACI (American Concrete Institute) (2015). "Guide for the Design and Construction of Concrete Reinforced with FRP Bars." *ACI 440.1 R-15*, Detroit, Michigan.

Bailiss, J. (2006). "Fabric-formed concrete beams: Design and analysis." MEng, University of Bath, Bath.

Boden, T., Marland, G., and Andres, R. (2013). "Global, Regional, and National Fossil-Fuel CO2 Emissions.", Carbon Dioxide Information Analysis Center (CDIAC), Oak Ridge National Laboratory, US Department of Energy,, Oak Ridge, Tenn., USA.

BSI (British Standards Institution) (2004). "Design of Concrete Structures: Part 1-1: General Rules and Rules for Buildings." *BS EN 1992-1-1:Eurocode 2*, London.

BSI (British Standards Institute) (2012). "Testing hardened concrete Shape, dimensions and other requirements for specimens and moulds." *BS EN 12390-1*, London.

BSI (British Standards Institute) (2009). "Testing hardened concrete: Compressive strength of test specimens." *BS EN 12390-3*, London.

CSA (Canadian Standards Association) (2012). "Design and construction of building structures with fibre-reinforced polymers." *CSA S806-12*, Ontario, Canada.

Darby, A., Ibell, T., Tallis, S., and Winkle, C. (2007). "End anchorage technique for internal FRP reinforcement." *Proceedings of Fibre-Reinforced Polymers for RC Structures (FRPRCS-8)*.

Field, C. B. (2014). *Climate change 2014–Impacts, adaptation and vulnerability: Regional aspects*, Cambridge University Press.

Garbett, J., Darby, A., and Ibell, T. J. (2010). "Optimised Beam Design Using Innovative Fabric-Formed Concrete." *Advances in Structural Engineering*, 13(5), 849-860.

Hashemian, F. K. (2012). "Structural behaviour and optimization of moment-shaped reinforced concrete beams." PhD, University of Manitoba (Canada).

Hawkins, W., Orr, J., Shepherd, P., Ibell, T., and Bregulla, J. "Thin-shell textile-reinforced concrete floors for sustainable buildings." *Proc., Proceedings of IASS Annual Symposia*, International Association for Shell and Spatial Structures (IASS), 1-9.

Kostova, K., Ibell, T., Darby, A., and Evernden, M. "Novel splayed anchorage system for internally reinforced concrete members." *Proc., 11th International Symposium on Fiber Reinforced Polymer for Reinforced Concrete Structures (FRPRCS-11)*.

Kostova, K. Z. (2016). "Design and constructability of fabric-formed concrete elements reinforced with FRP materials." PhD, University of Bath.

Lee, S. H. (2011). "Study of construction methodology and structural behaviour of fabric-formed form-efficient reinforced concrete beam." PhD, University of Edinburgh.

Mara, V., Haghani, R., and Harryson, P. (2014). "Bridge decks of fibre reinforced polymer (FRP): A sustainable solution." *Construction and Building Materials*, 50, 190-199.

Orr, J. (2012). "Flexible formwork for concrete structures." PhD, University of Bath.

Orr, J., Drewniok, M. P., Walker, I., Ibell, T., Copping, A., and Emmitt, S. (2019). "Minimising energy in construction: Practitioners' views on material efficiency." *Resources, Conservation and Recycling*, 140, 125-136.

Orr, J. J., Darby, A., Ibell, T. J., Evernden, M., and Otlet, M. (2011). "Concrete structures using fabric formwork." *The Structural Engineer*, 89(8), 20-26.

Spadea, S., Orr, J., and Ivanova, K. (2017). "Bend-strength of novel filament wound shear reinforcement." *Composite Structures*, 176, 244-253.

Spadea, S., Orr, J., Nanni, A., and Yang, Y. (2017). "Wound FRP shear reinforcement for concrete structures." *Journal of Composites for Construction*, 21(5), 04017026.

Teychenné, D. C., Franklin, R. E., and Erntroy, H. C. (1975). *Design of normal concrete mixes*.

Thirion, C. (2013). "Putting the material in the right place: Investigations into the sustainable use of structural materials to reduce the initial embodied environmental impact of building structures." PhD, UCL (University College London).

Veenendaal, D., West, M., and Block, P. (2011). "History and overview of fabric formwork: using fabrics for concrete casting." *Structural Concrete*, 12(3), 164-177.

West, M. (2016). *The fabric formwork book: Methods for building new architectural and structural forms in concrete*, Routledge.

Yang, Y., Orr, J., and Spadea, S. (2018). "Shear Behavior of Variable-Depth Concrete Beams with Wound Fiber–Reinforced Polymer Shear Reinforcement." *Journal of Composites for Construction*, 22(6), 04018058.

**Figure1**

**Click here to download high resolution image**

Figure2

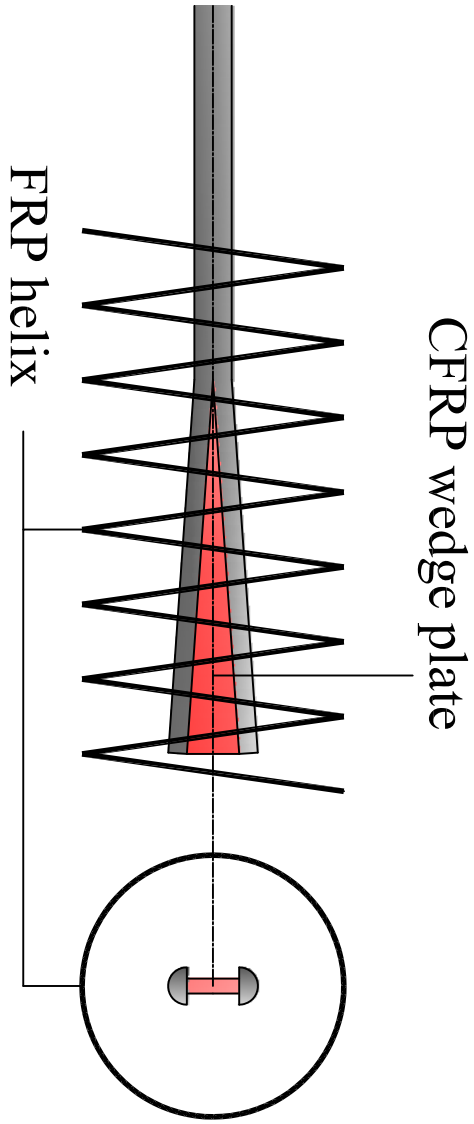


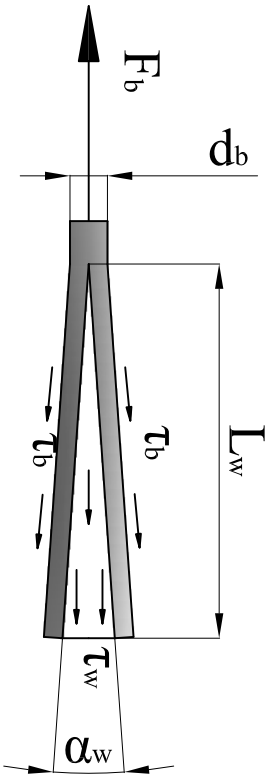

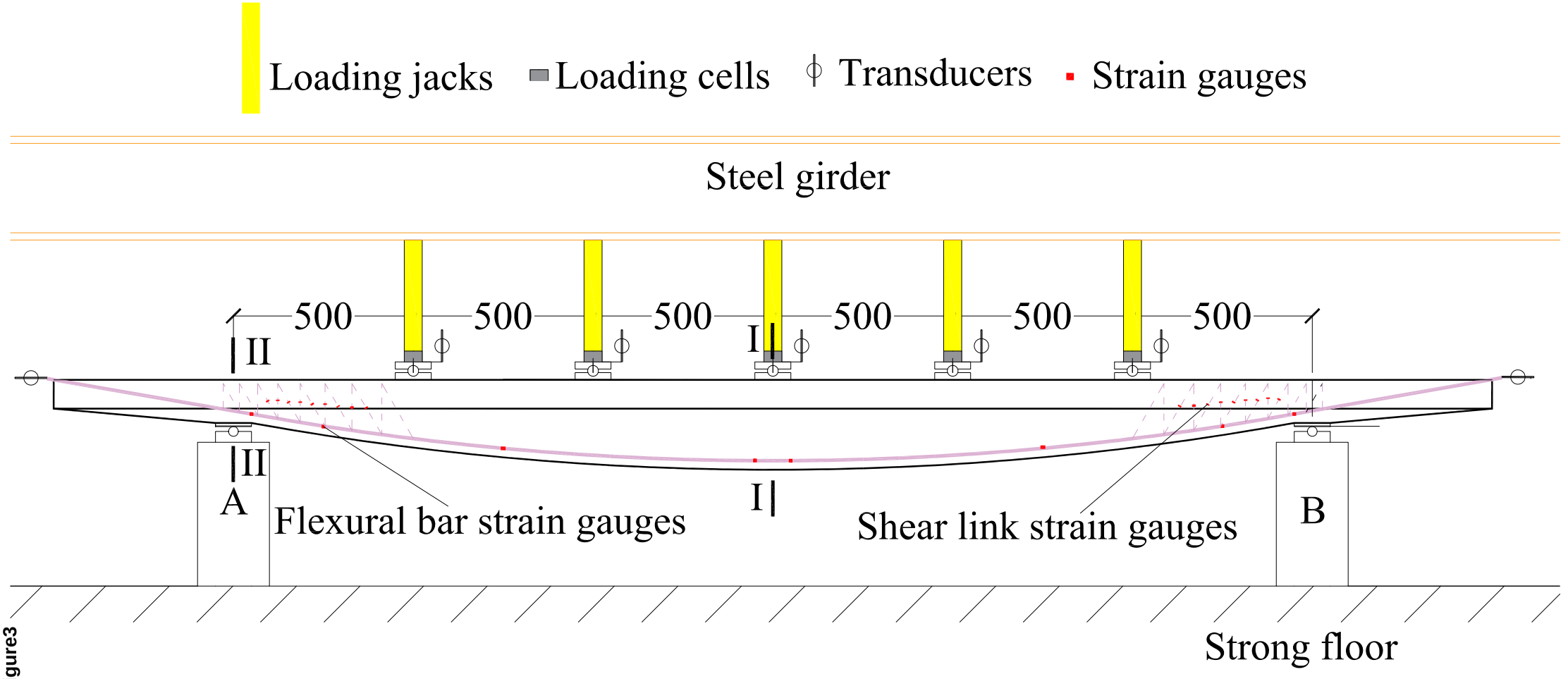
Loading jacks
Loading cells
Transducers
Strain gauges
Steel girder
500
500
500
500
500
500
II
I
II
I
A
B
Flexural bar strain gauges
Shear link strain gauges
Strong floor

Figure3

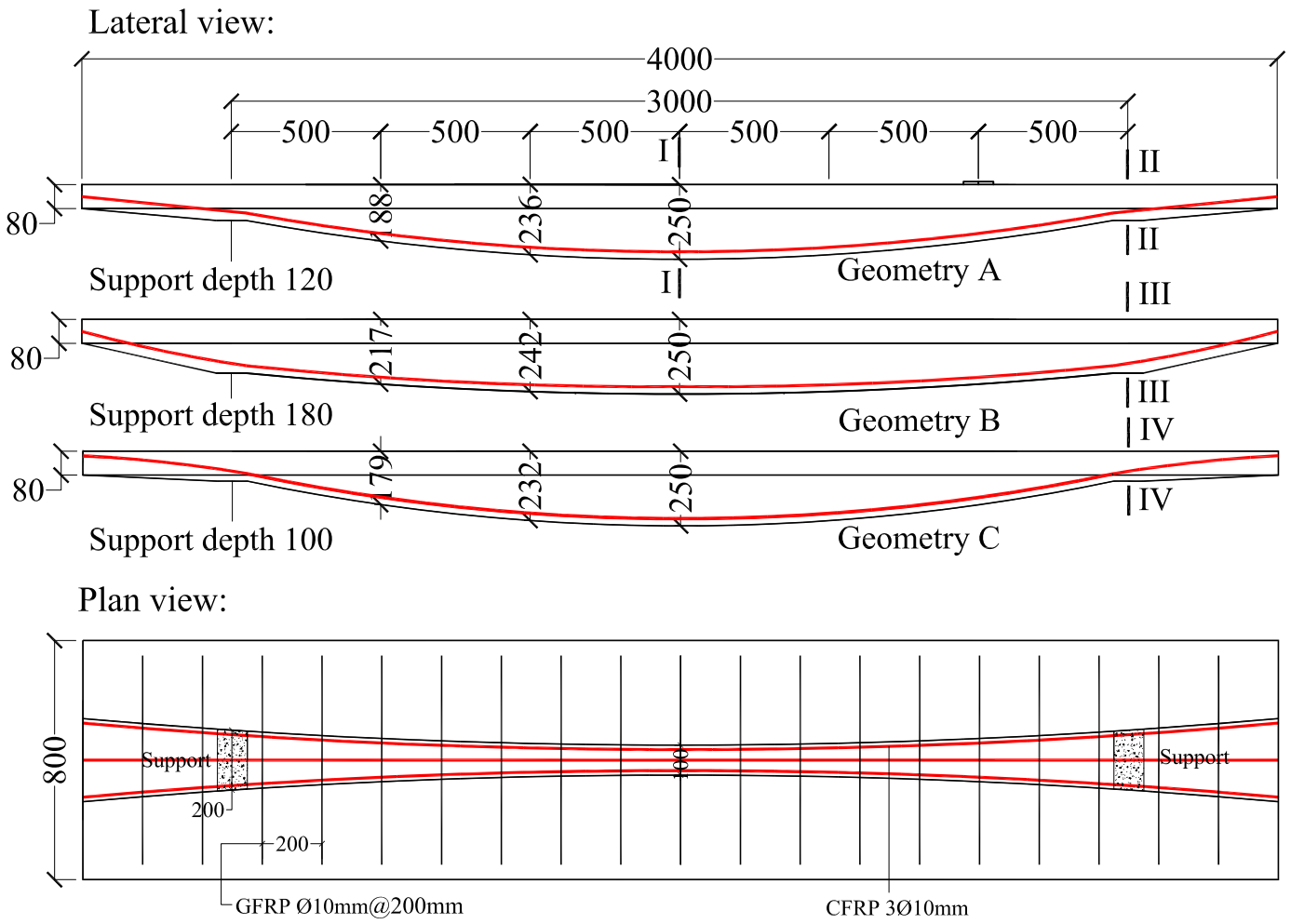
Lateral view:
4000
3000
500
500
500
500
500
500
I
II
80
188
236
250
Support depth 120
Geometry A
II
III
80
217
242
250
Support depth 180
Geometry B
III
IV
80
179
232
250
Support depth 100
Geometry C
IV


Plan view:
800
Support
Support
200
200
100
GFRP Ø10mm@200mm
CFRP 3Ø10mm

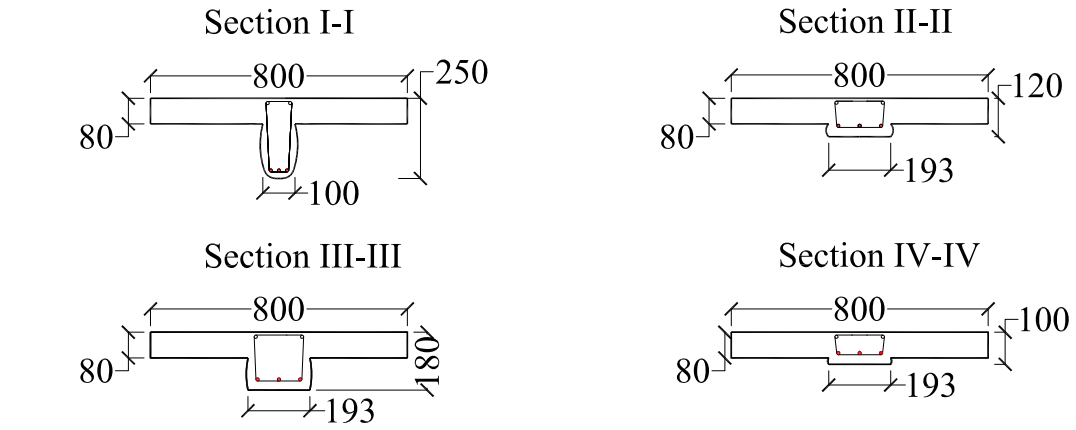
Cross sections:
Section I-I
800
250
80
100
Section II-II
800
120
80
193
Section III-III
800
80
180
193
Section IV-IV
800
100
80
193

Figure4

Figure5

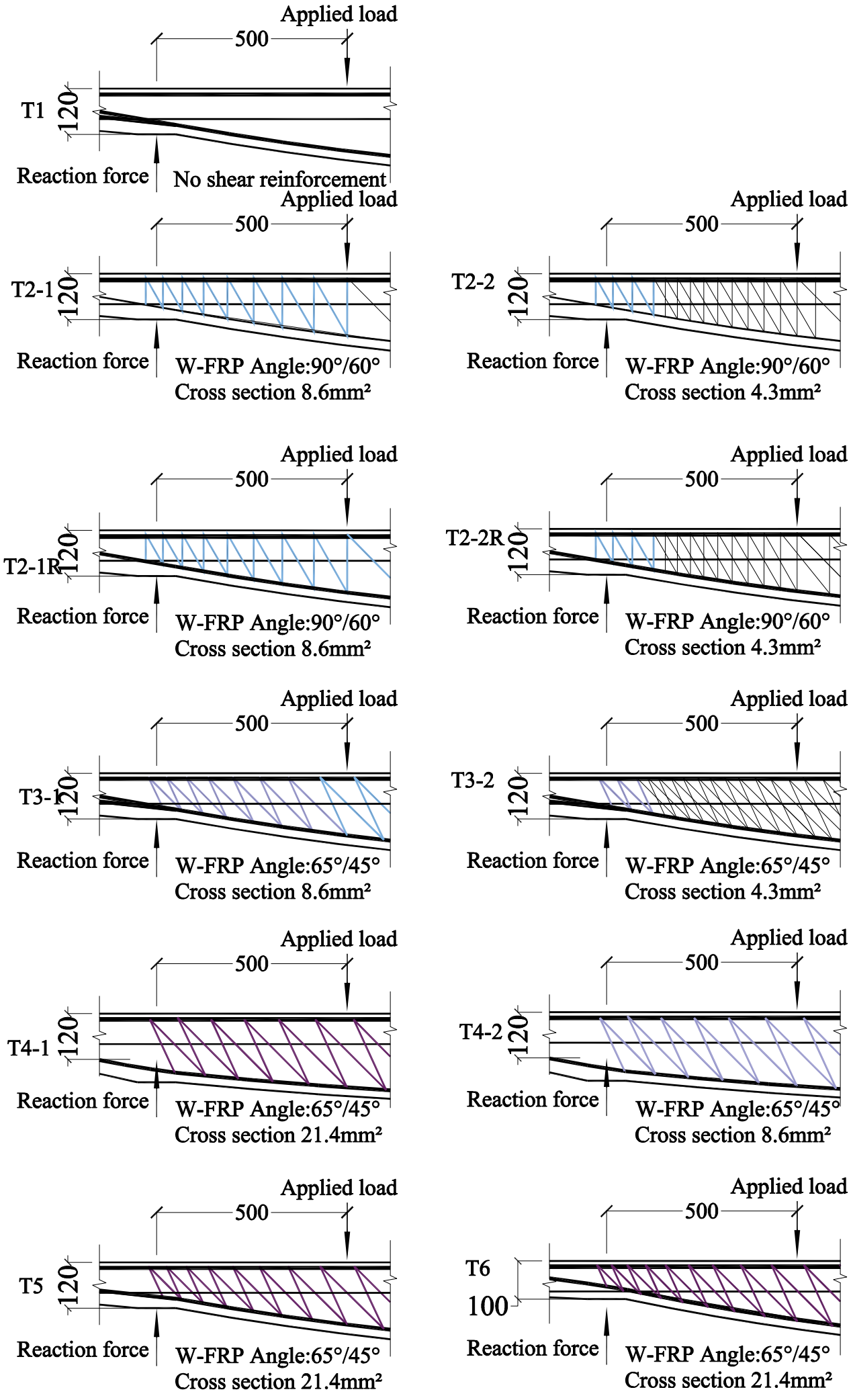
Applied load
500
T1
120
Reaction force
No shear reinforcement
Applied load
500
T2-1
120
Reaction force
W-FRP Angle:90°/60°
Cross section 8.6mm²
Applied load
500
T2-2
120
Reaction force
W-FRP Angle:90°/60°
Cross section 4.3mm²
Applied load
500
T2-1R
120
Reaction force
W-FRP Angle:90°/60°
Cross section 8.6mm²
Applied load
500
T2-2R
120
Reaction force
W-FRP Angle:90°/60°
Cross section 4.3mm²
Applied load
500
T3-1
120
Reaction force
W-FRP Angle:65°/45°
Cross section 8.6mm²
Applied load
500
T3-2
120
Reaction force
W-FRP Angle:65°/45°
Cross section 4.3mm²
Applied load
500
T4-1
120
Reaction force
W-FRP Angle:65°/45°
Cross section 21.4mm²
Applied load
500
T4-2
120
Reaction force
W-FRP Angle:65°/45°
Cross section 8.6mm²
Applied load
500
T5
120
Reaction force
W-FRP Angle:65°/45°
Cross section 21.4mm²
Applied load
500
T6
100
Reaction force
W-FRP Angle:65°/45°
Cross section 21.4mm²

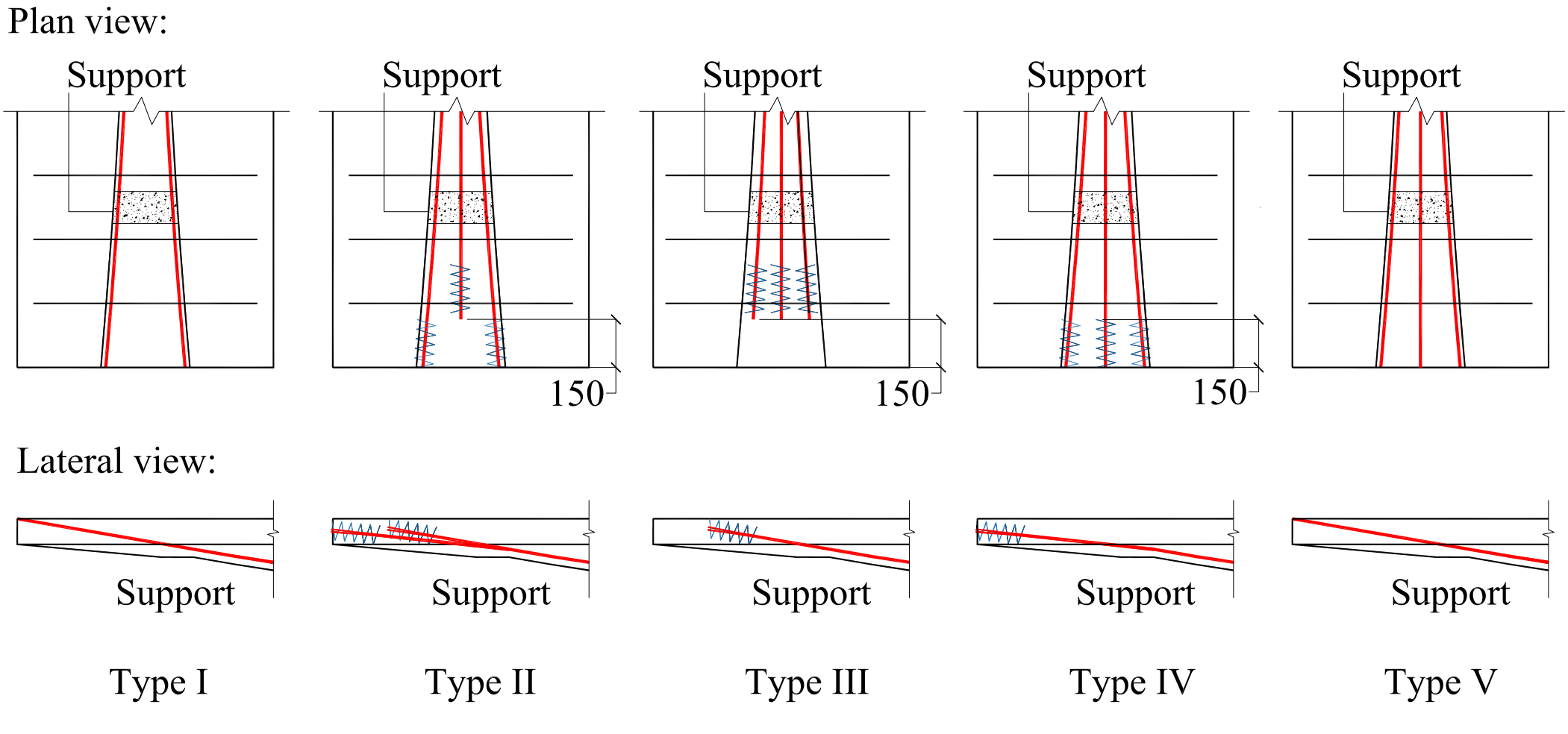
Plan view:
Support
Support
Support
Support
Support
150
150
150
Lateral view:
Support
Support
Support
Support
Support
Type I
Type II
Type III
Type IV
Type V

Figure6

Figure7
Click here to download high resolution image

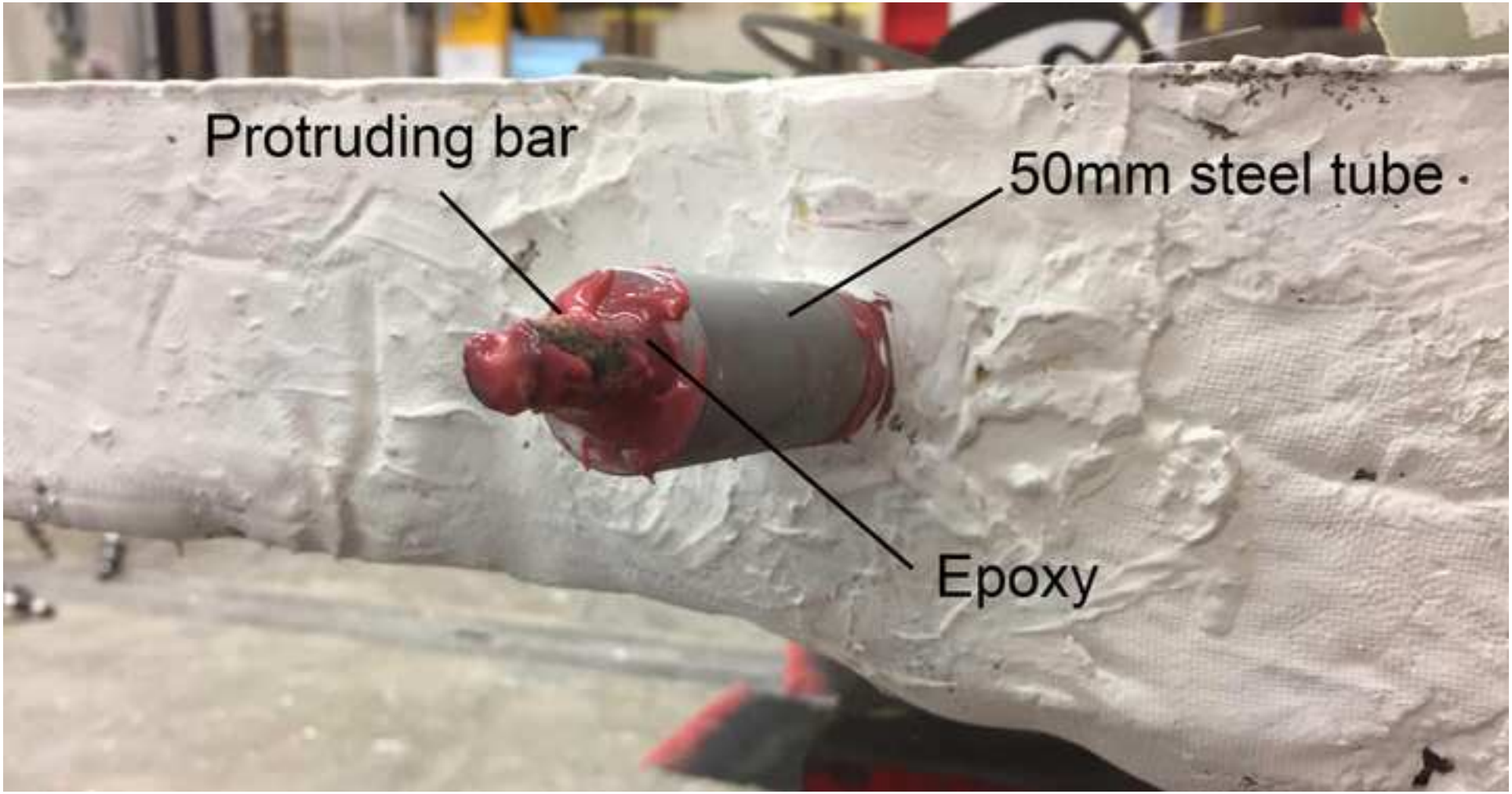

Figure8

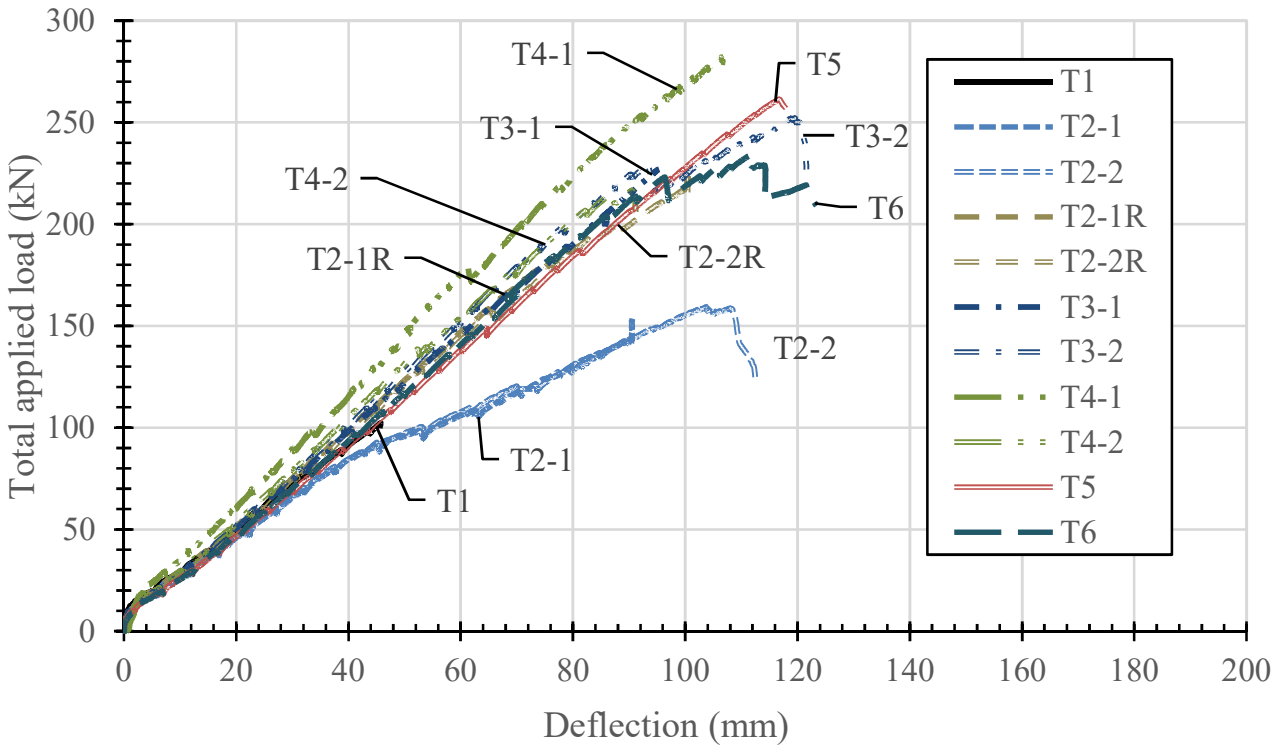
Total applied load (kN)
Deflection (mm)
0
50
100
150
200
250
300
0
20
40
60
80
100
120
140
160
180
200
T4-1
T5
T3-1
T3-2
T4-2
T6
T2-1R
T2-2R
T2-2
T2-1
T1
T1
T2-1
T2-2
T2-1R
T2-2R
T3-1
T3-2
T4-1
T4-2
T5
T6

**Figure9**

**Click here to download high resolution image**

**Figure9**

**Click here to download high resolution image**

**Figure10**

**Click here to download high resolution image**

Figure10

Click here to download high resolution image

**Figure10**

**Click here to download high resolution image**

Figure10

Click here to download high resolution image

**Figure11**

**Click here to download high resolution image**

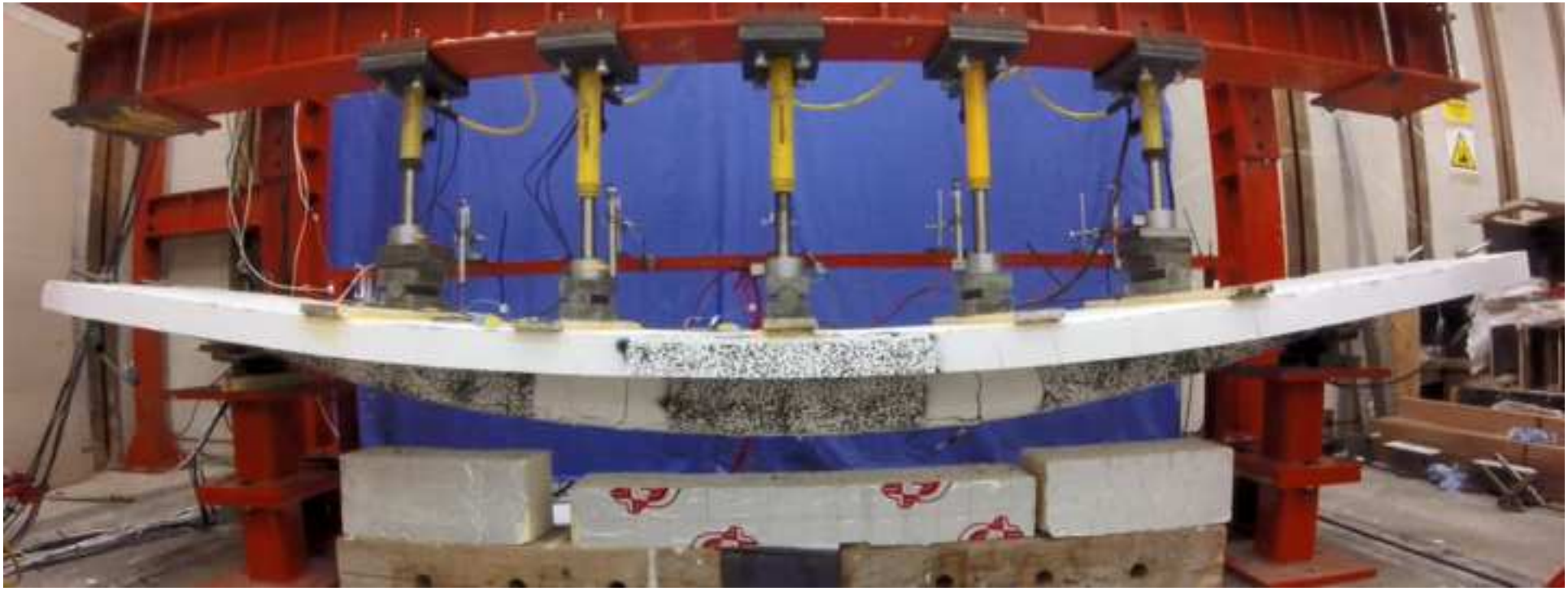

**Figure11**

**Click here to download high resolution image**

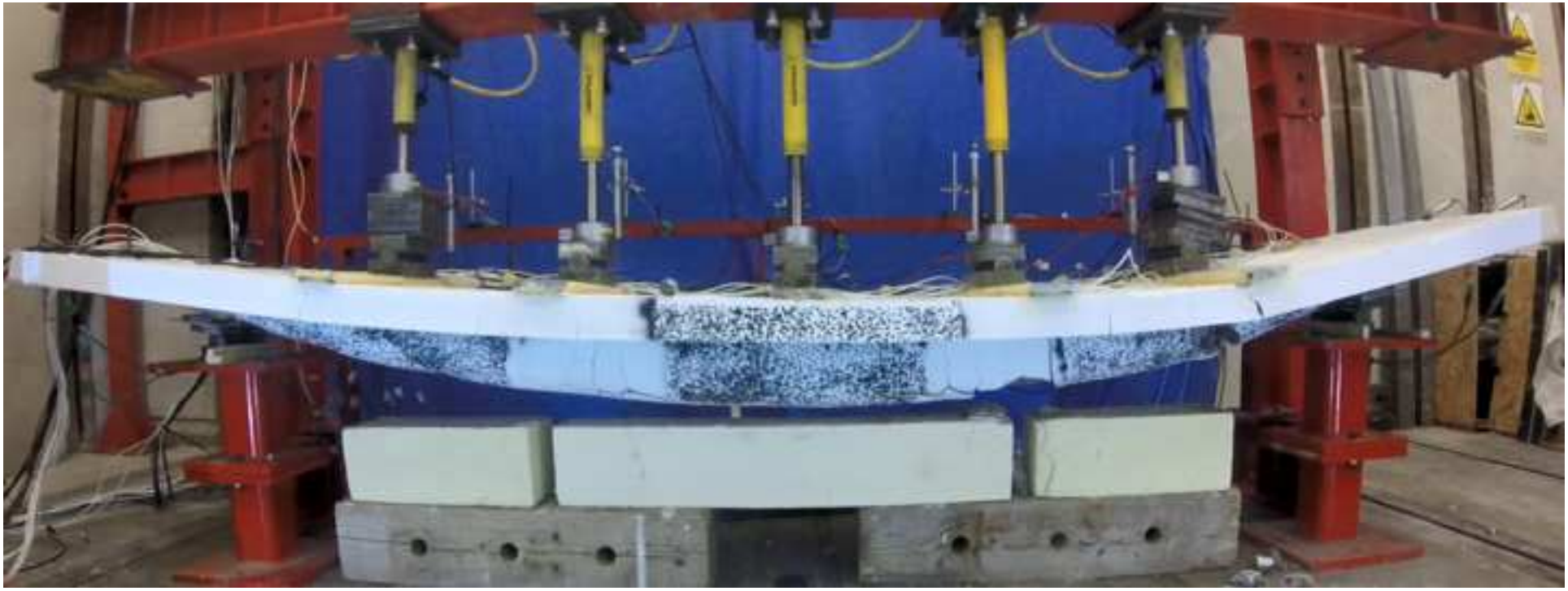

**Figure11**

**Click here to download high resolution image**

**Figure11**

**Click here to download high resolution image**

**Figure11**

**Click here to download high resolution image**

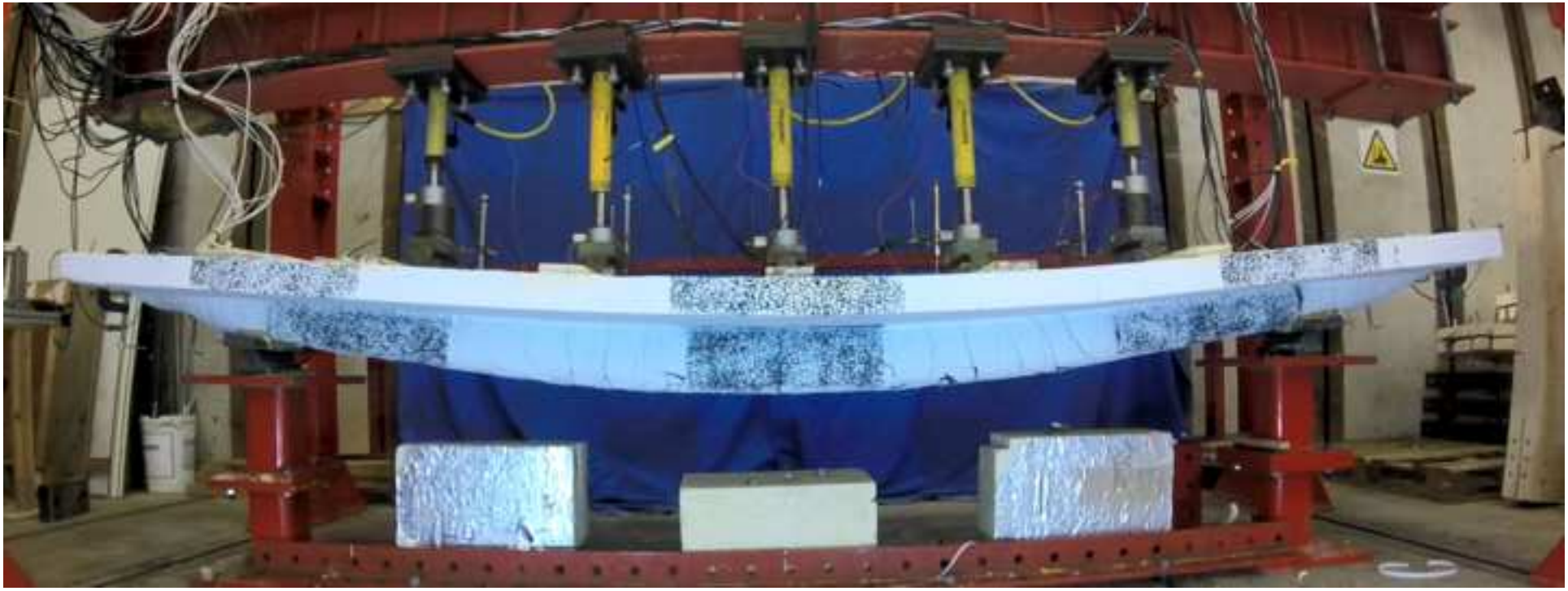

**Figure12**

**Click here to download high resolution image**

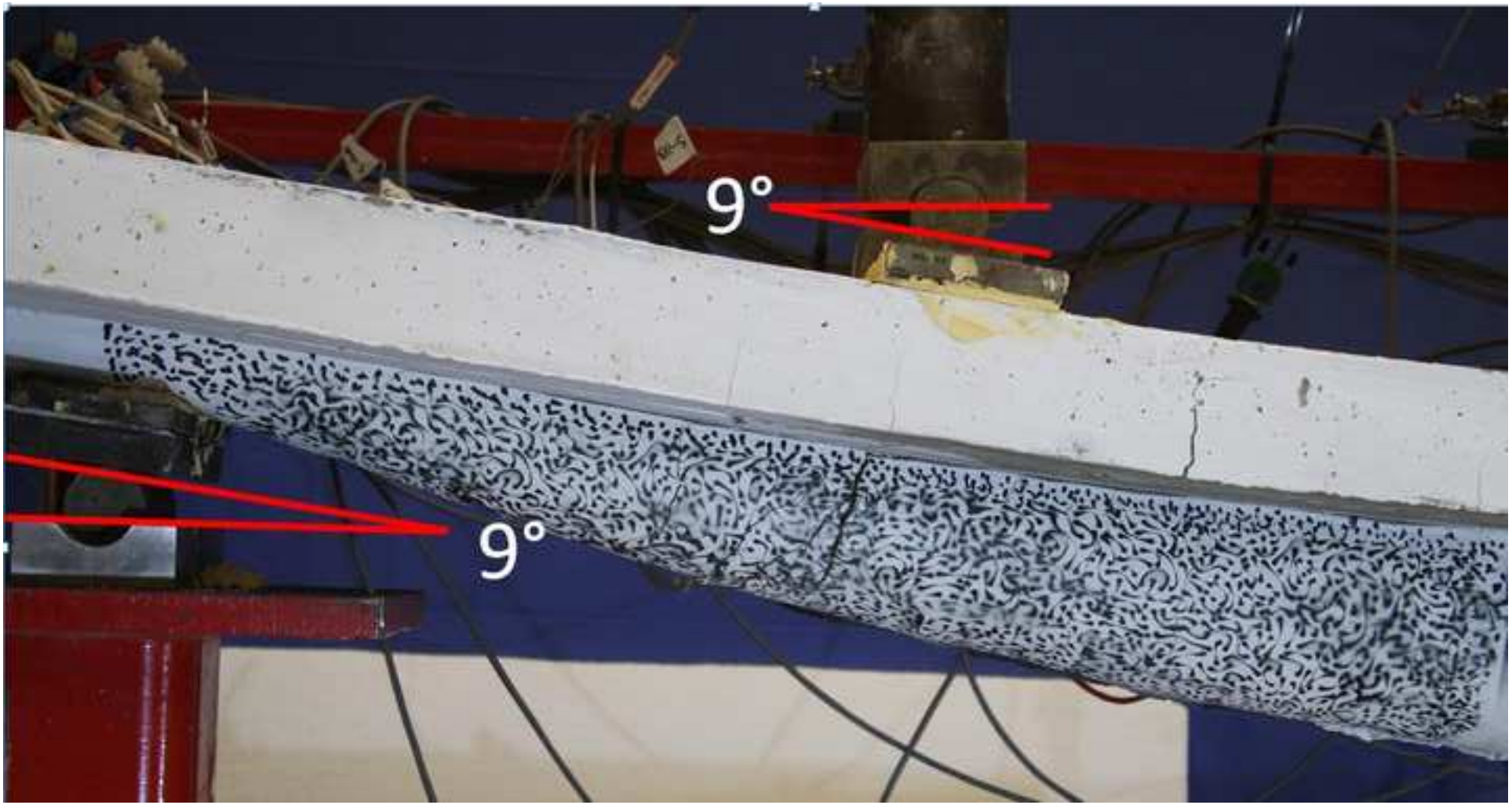

**Figure13**

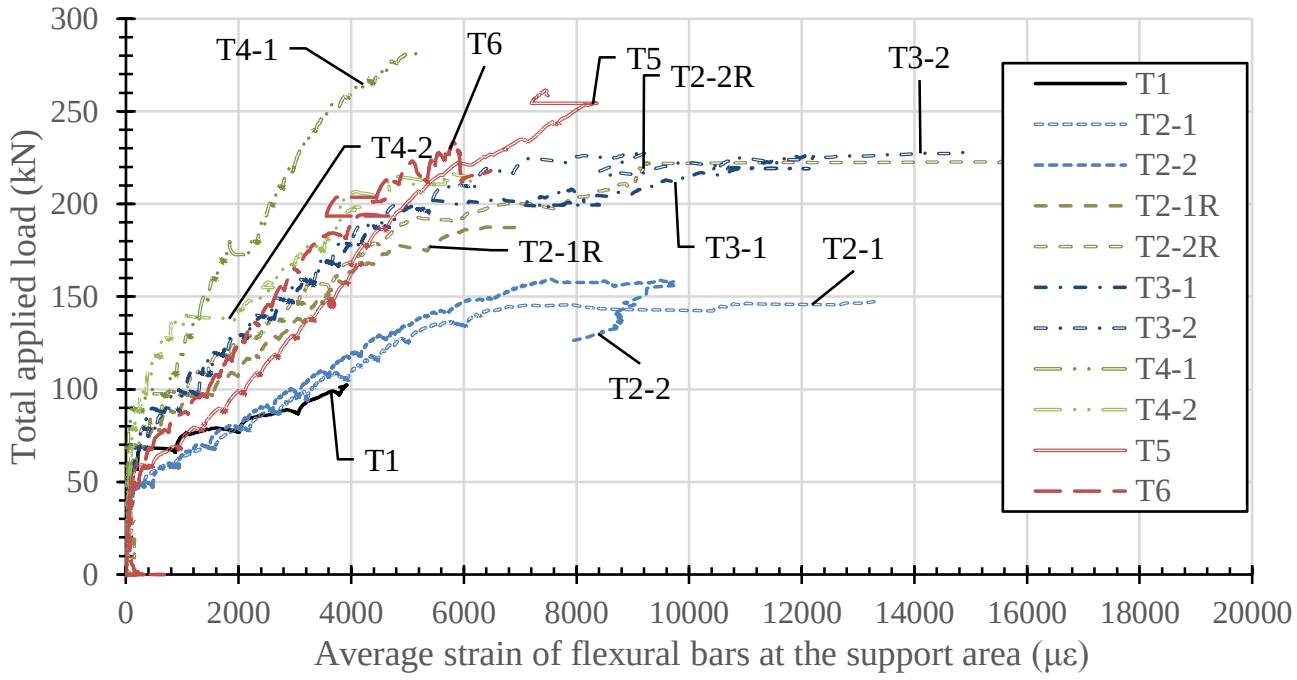
Total applied load (kN)
Average strain of flexural bars at the support area (με)
0
50
100
150
200
250
300
0
2000
4000
6000
8000
10000
12000
14000
16000
18000
20000
T4-1
T6
T5
T2-2R
T3-2
T4-2
T2-1R
T3-1
T2-1
T2-2
T1
T1
T2-1
T2-2
T2-1R
T2-2R
T3-1
T3-2
T4-1
T4-2
T5
T6

Figure14

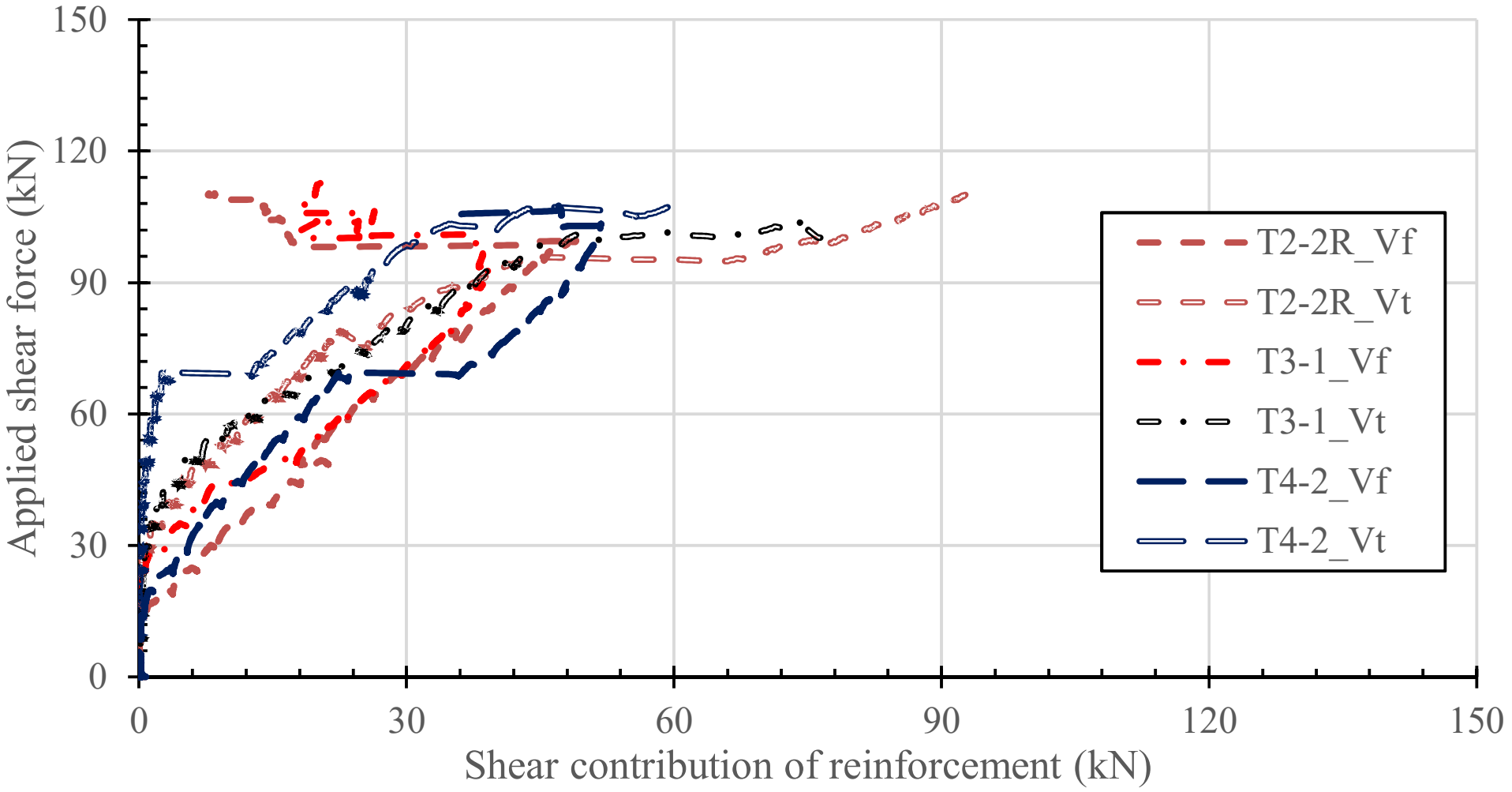
150
120
90
60
30
0
Applied shear force (kN)
0
30
60
90
120
150
Shear contribution of reinforcement (kN)
T2-2R_Vf
T2-2R_Vt
T3-1_Vf
T3-1_Vt
T4-2_Vf
T4-2_Vt

Figure15

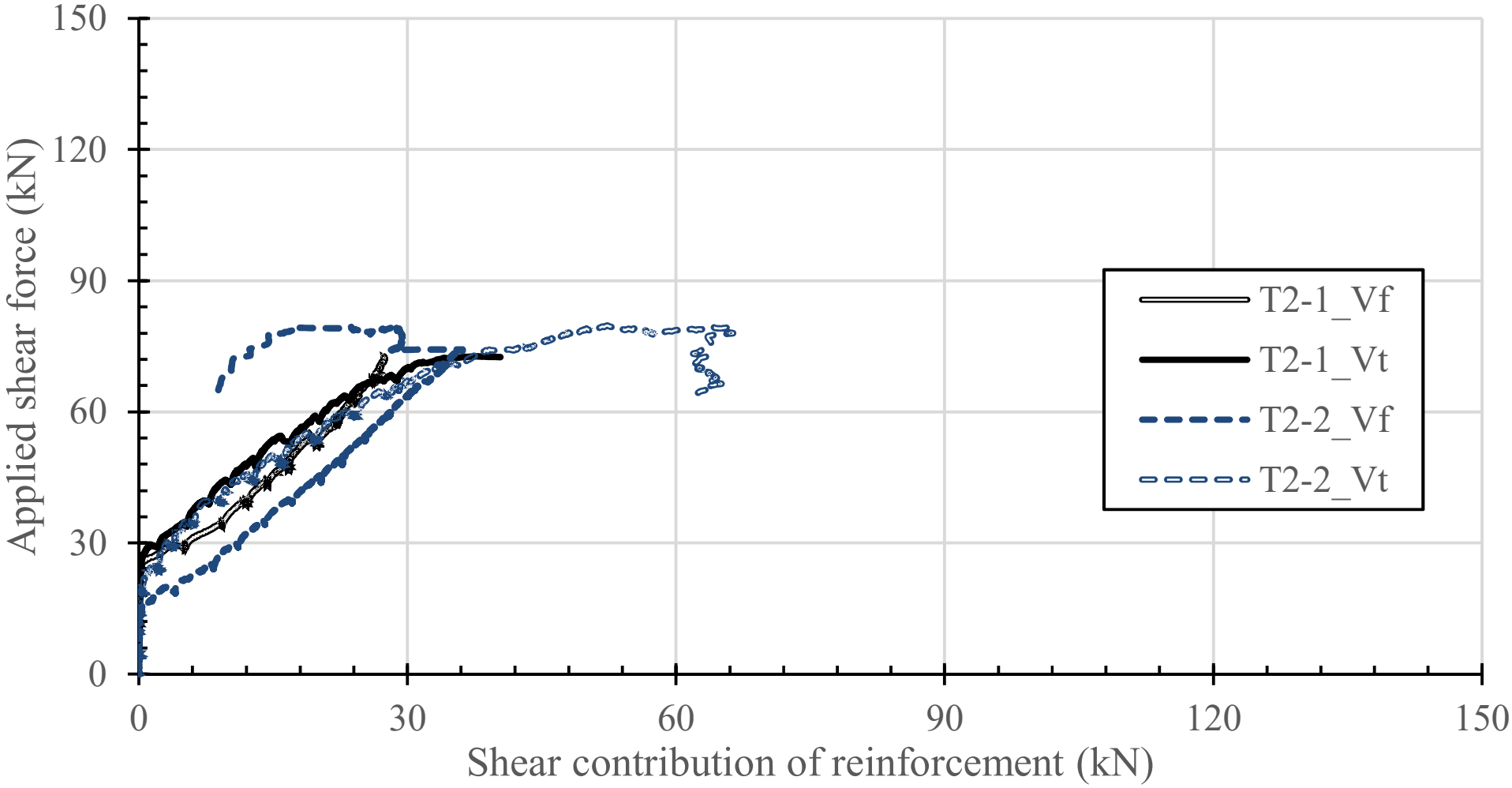
150
120
90
60
30
0
Applied shear force (kN)
0
30
60
90
120
150
Shear contribution of reinforcement (kN)
T2-1_Vf
T2-1_Vt
T2-2_Vf
T2-2_Vt

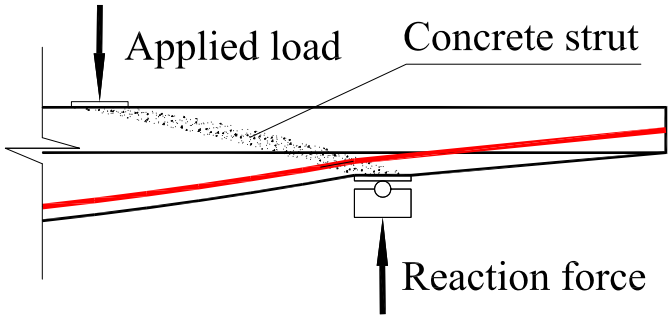


T1, T2, T2R and T3

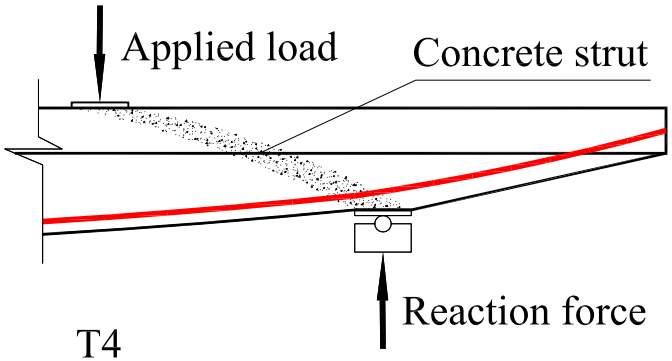


T4

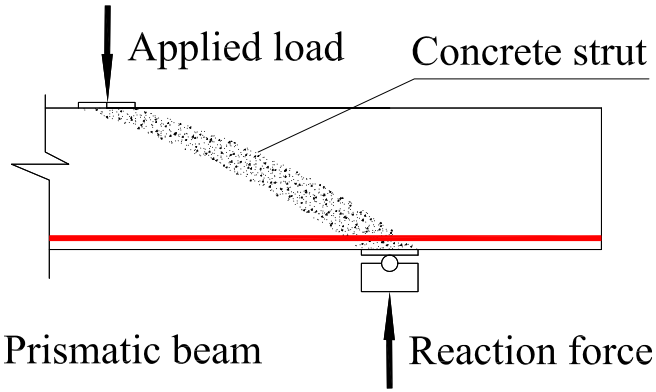


Prismatic beam

Figure16